Nanoscale Channels and Tunnels in Surface-Modified Poly(dimethylsiloxane)

by

Kristen L. Mills

A dissertation submitted in partial fulfillment
of the requirements for the degree of
Doctor of Philosophy
(Mechanical Engineering)
in The University of Michigan
2008

Doctoral Committee:

Professor Michael D. Thouless, Co-Chair
Associate Professor Shuichi Takayama, Co-Chair
Professor Ellen M. Arruda
Professor Tresa M. Pollock
Associate Professor Krishnakumar R. Garikipati

Dedication

To my parents

Acknowledgements

I would be remiss if I did not thank several people without whom I would not have come this far.

Words cannot express how much I appreciate the unwavering support and encouragement from my advisor, **Professor Michael Thouless**.

I could not find a better friend in this world than **Andrew Ickes**.

Dr. Jessica Schroeder has provided me with very thoughtful mentoring and friendship.

My collaborations with the co-authors on this work – **Professor Shuichi Takayama** (Chapters 2-4), **Dr. Xiaoyue (Terry) Zhu** (Chapter 2), **Dr. Dongeun (Dan) Huh** (Chapter 4), and **Dr. Tomoyuki Uchida** (Chapter 3) – have been very productive, interesting, and fun.

Finally, I thank **Dr. Laura Monschau** for helping me to navigate the final year.

Table of Contents

List of Figures

Chapter:

Abstract

Exposing the elastomer polydimethylsiloxane (PDMS) to oxygen plasma creates a very thin, stiff, and brittle surface-modified layer. Nano-scale crack patterns can be introduced to this layer with tensile stress. To optimize the pattern formation for a specific nano- or bio-technology research application, the surface-modified layer must be fully characterized. A characterization method was developed, using a combination of experiments and finite-element modeling. Phase imaging and nanoindentation with the atomic force microscope showed that the surface-modified layer was graded over approximately 200 nm, with an elastic modulus at the surface approximately ten-times that of the unmodified PDMS. Finite-element analyses indicated that the toughness of the surface-modified layer is extremely low (0.1 – 0.3 J/m^2) and that the embrittlement extends 100 – 400 nm below that of the measured layer thickness, signifying that the cracks may extend deeper than the apparent layer thickness.

Variations of the nanocrack-patterning method were used to produce functional nanoscale patterns. First, surface-modified PDMS cubes and microspheres were uniaxially compressed causing their surfaces to be decorated with nanocrack patterns. Pattern formation, due to the distribution of tensile stresses in the surface-modified layer, on the cube surfaces was associated with friction at the contacts with the platens; whereas, for the microspheres it could exclusively be attributed to the changing cross-sectional area along the axis of compression. Second, an array of parallel tunnel cracks

was produced in the surface-modified layer, when sandwiched between PDMS substrates, with an applied uniaxial tensile strain. The tunnel cracks functioned as tunable nanochannels when they connected pre-patterned microchannel reservoirs. Modulated fluidic transport of single particles between the reservoirs was demonstrated and electrical resistance measurements confirmed the nanochannel adjustability (from approximately 1 μm wide to completely closed).

Due to the compliance of PDMS, surface forces were able to cause the channel and tunnel cracks to close, or heal, upon removal of applied tensile strain. The self-adhesion of the nanochannel walls due to surface forces was studied and the conditions for collapse were determined. A method for determining and applying a non-uniform traction on the surface of bodies that are interacting due to surface forces was developed.

Chapter 1

Introduction

The common theme to the research presented in this dissertation is the nano-scale cracking of a very thin, stiff, brittle surface-modified layer on a compliant substrate. The initial motivation to study these nanocracks was provided by the desire to use them as a quick and easy method of creating functional nano-scale surface patterns to study cellular adhesion (*1*). In order to successfully design functional nano-scale patterns using these cracks, the properties of the film in which they are created need to be determined and understood with respect to the method with which it is produced. This concern is addressed first in Chapter 2 followed in Chapters 3 and 4 by a demonstration of two further variations on pattern creation using the nanocracks. The intended applications for these patterns are both discussed and demonstrated. Finally, the material system in which the nanocracks are created is unique in that the substrate material is compliant enough to be noticeably effected by surface forces. It was experimentally observed that these surface-forces acted to partially – and in some cases fully – close or heal the cracks when energetically favorable. These observations prompted a general study on adhesion due to surface forces which is discussed in Chapter 5.

The substrate material, poly(dimethylsiloxane) (PDMS), is an elastomer that is commonly used in biomedical research due to its biocompatibility. It is easily cast as a liquid prepolymer onto patterned molds microfabricated in silicon creating the patterns that are the basis of many microfluidic devices. PDMS, in its unmodified state, is hydrophobic. This inherent hydrophobicity is not conducive to achieving good wetting of fluids, especially in the confined volumes of microfluidic devices. Therefore, a common method for considerably increasing the surface energy is to treat the PDMS with plasma oxygen for a short period of time: generally on the order of 30 seconds to one minute. It has become well known that, in addition to rendering the surface hydrophilic, the exposure to plasma oxygen also has the effect of "damaging" the surface, much in the same way that environmental exposure, over time, embrittles rubber materials like rubber bands (*2, 3*). In fact, other methods sometimes used to achieve similar results on PDMS surfaces include ultraviolet and ozone (UV/ozone) radiation treatment (*4*) as well as exposure to corona discharges (*5*). Surface chemical analyses directly following plasma treatment have shown that there is an increase in the number of Si–O bonds, usually an Si atom bound to 3 or 4 oxygen atoms (SiO_x) (*6*). Therefore, this sometimes-termed silica-like layer is significantly stiffer than the bulk PDMS substrates and exhibits the classical behaviors of such a layered system when stress is applied to the system, namely, buckling and cracking of the thin film.

The ordered patterns of nano-scale cracks in the surface-modified layer have proven to be a useful tool for biological studies such as cellular adhesion and behavior (*1*) and nanofluidic channels for single molecule studies (*7*). This is partly due to the biological compatibility of the material, but also a set of conditions making this system

unique: its mechanical properties, the length scale over which the sizes of the cracks may be dynamically changed, and the difference in the surface properties between the unmodified and modified states. Since the cracks have been shown to be functional, it is desired to be able to predict – based on a given set of material properties, plasma treatment conditions, and stress state – what the likely crack patterns will be, even design systems with a certain crack pattern. The tools necessary to have such a design capability exist in the mechanics of thin films field (*8-12*). However, to be able to apply them requires the knowledge of the material properties and thickness of the layer. The second Chapter of this dissertation addresses the challenges that arise when the task of determining these properties is undertaken and discusses the estimates made of these properties from the results of a series of experiments.

The ability to instantaneously generate controlled nano-scale patterns on a clean surface is very interesting as well as useful for the micro- and nano- engineering of materials. Specifically, the ability to quickly and easily produce specific designs of patterns on micro- and nano-scale particles for directed self-assembly (*13-15*) would be advantageous. The patterning of small objects that are not flat presents a challenge for conventional bottom-up micro- and nano-fabrication techniques. By taking advantage of the ability to produce crack patterns in response to a tensile stress in the surface-modified layer on PDMS, a compression technique was developed to produce crack patterns on 3D micro- and nano-particles. Chapter 3 introduces the technique that was used and discusses the effects of the geometrical parameters of the particles on the resulting crack patterns.

As previously mentioned, the cracking of the surface-modified layer on PDMS has been used as the basis to fabricate size-adjustable nanochannels. In recent years, partly due to the success of micro-fluidics, several techniques have been developed for fabrication of nano-channels. Most methods are based on standard nanofabrication techniques in silicon or silicon nitride and are time consuming and produce static nanochannels (*16*). Nonetheless, these nanochannels have been instrumental in studies that have elucidated the behavior and mechanics of single molecules of DNA (*17-21*). These studies would be enhanced and others, such as dynamic sieving of different-sized molecules, would be made possible with the ability to adjust the size of the nanochannels. Chapter 4 presents a very simple and effective method for producing nanochannels in the surface-modified layer of PDMS via tunnel cracking of the surface-modified layer when it is constrained between two substrates.

Finally, observations made during the work on the nano-channels and tunnels have shown that, upon the removal of applied stress, the channels at least partially heal and, in the case of the tunnels, nearing complete removal of the applied stress, their presence is imperceptible using a high-magnification optical microscope. The relative compliance of the substrate together with the very small length scale presents the favorable condition for the adhesion of the crack walls due to surface forces. The stability of micro- and nano-scale structures against deformations and collapse due to surface forces has been considered for the replication of high-aspect-ratio patterns in compliant materials (*22, 23*) as well as the deformation and collapse of soft-lithographic stamps (*24*). In the case of the latter and analyses similar to it, the only geometry considered is a raised rectangular stamp feature. Additionally, initial assumptions are

made about how the adhesion will proceed. In Chapter 5, the collapse of the included features of stamps or nanochannels is studied first for the triangular-shaped nanochannels produced in PDMS followed by the presentation of the development of a method that was devised for studying the adhesion of these small scale features irrespective of their geometry.

Chapter 2

The mechanical properties of a surface-modified layer on poly(dimethylsiloxane)

2.1 Introduction

Polydimethylsiloxane (PDMS), an elastomer which is transparent at visible wavelengths, is a very common material used in a myriad of applications in bioengineering, electronics, and MEMS. Specifically, some of these applications include micromachined mechanical and chemical sensors (*25*), stamp material for soft lithography (*26, 27*), and microfluidics devices (*28-30*). PDMS is widely used because it is biologically inert, gas permeable, an insulator, and good for rapid prototyping of devices. However, for applications where laminar flow or wetting of fluids is desired, the inherent hydrophobicity of the PDMS surface is not ideal. Therefore, the surface of PDMS is often made hydrophilic by oxidation techniques which emulate environmental exposure (*2, 3*), only in an expedited manner. In addition to changing the surface chemistry, oxidation creates a stiff, thin surface-modified layer (*31-33*). The oxidized PDMS exhibits mechanical behaviors that are characteristic of elastically-mismatched layered materials, but at the nano-scale. Specifically, moderate uniaxial tensile strains (for an elastomer) produce periodic parallel cracks in the stiff surface-modified layer (*1*), and compressive strains induce surface buckling (*31*).

This behavior has proved to be useful for applications for which patterns at a nano-scale are desired. For example, a recent study showed that when the nano-cracks in the surface-modified layer of oxidized PDMS are decorated with adhesive proteins, they can support the growth and modulation of cells (*1*). It has also been shown that these cracks can be easily produced on micro- and nano-scale 3D objects such as cubes and spheres (see Chapter 3). If the nanocracks on these 3D objects can also be decorated with adhesive proteins or molecules they could possibly provide a useful 3D environment with which cellular behavior may be studied. Additionally, nano-crack patterning has been used as the platform for creating reconfigurable nano-channels (*7*). A method for producing these nanochannels and some demonstrations of their functionality is presented in Chapter 4. For these applications it would be particularly advantageous to be able to design patterns of nano-cracks and to understand how the patterns would respond to applied strains. The basic framework for such design methodologies is provided by the traditional tools of thin-film mechanics. However, this requires knowledge of the mechanical properties of the layered system, including the elastic properties and toughness of both the surface-modified layer and the substrate, and the thickness of the surface-modified layer. While the bulk material (the PDMS substrate) can be easily characterized using standard tests, the surface-modified layer is too thin for its properties to be measured directly. As a result, there is a significant challenge in determining the properties of the surface-modified layer on PDMS.

Previous work has indicated that a surface-modified layer created by plasma oxidation or by exposure to ultraviolet/ozone radiation is less than a micron thick and can have an elastic modulus of anywhere between 4 and 750 MPa (*4, 31-33*). Two

different techniques have been used to measure the thickness of the surface-modified layer. First, a scanning electron microscope was used to image the cross-section of PDMS that had been exposed to plasma oxygen for 15 minutes (*31*). A demarcation between two regions was observed approximately 0.5 μm below the free surface, and this was taken to be the depth of the surface-modified layer. Second, a combination of neutron reflectometry and X-ray photoelectron spectroscopy was used to measure the thickness of the surface-modified layer; and, it was determined that there was a decrease in the thickness from 160 nm after 80 seconds of exposure to oxygen plasma, to 130 nm after 180 seconds of exposure (*33*).

Estimates of the elastic modulus of the surface-modified layer include those calculated from the buckling wavelength of a compressed surface-modified layer and those calculated from nanoindentation results. When a stiff layer buckles on an elastic foundation there is a characteristic wavelength that depends on the modulus and thickness of the layer and on the modulus of the substrate. Having estimated the layer thickness associated with 15 minutes of plasma oxidation, Bowden *et al.* (*31*) used this result to estimate the elastic modulus of the surface layer to be about 750 MPa. Nanoindentation analyses based on indentation curves generated with the atomic force microscope have produced estimates for the stiffness of surface-modified layers created using ultraviolet/ozone radiation for periods up to 90 minutes. The values of these estimates are 4–11.2 MPa (*4*) and 15–87 MPa (*32*). However, the limitations of using indentation techniques to measure the modulus are well recognized when a stiff layer is on top of a compliant substrate, as the indentation is affected by the substrate over the full range of indentation depths (*34, 35*).

In this Chapter, an investigation of the material properties of plasma-oxidized PDMS is presented—an integral aspect of understanding the mechanics of nano-cracking in this system. The properties of the PDMS are straightforward to determine with established experimental methods and are presented in Section 2.2. Addressing the challenge of assessing the material properties of the surface-modified layer, Section 2.3 demonstrates a two-step method, using the atomic-force microscope, to determine its thickness and elastic modulus. If different oxidizing conditions were to be explored, it is envisioned that this method would be a relatively quick and easy technique to assess the properties of the resulting surface-modified layer. Finally, in Section 2.4 the fracture behavior of a surface-modified layer is discussed in the light of the measured material properties.

2.2 Materials preparation and properties of the bulk PDMS

2.2.1 Materials preparation

Initial studies showed that both the ratio of the polymer to the curing agent and the curing schedule affected the constitutive behavior of the resulting elastomer. Therefore, care was taken to ensure that all experiments were performed with PDMS that was produced using the same mixing and curing parameters. In particular, Dow Corning (Sylgard 184) PDMS was prepared with a ratio of 10 parts of polymer to 1 part of curing agent. The liquid polymer was poured into glass Petri dishes and then cured at 60°C for three hours followed by 12 hours at 150°C. The resulting thickness of the PDMS sheets used throughout this study was 2.0 ± 0.2 mm.

The PDMS was oxidized by exposing the cured sheets to oxygen plasma in the Pyrex chamber of a plasma etcher.[1] A maximum power of 100 W was used for a period of four minutes with a pure oxygen environment at a relative vacuum of about 300 mtorr. However, precise control of the oxidation conditions could not be guaranteed between different oxidation runs. In the results that follow, it will be indicated when comparisons are being made between specimens oxidized together or in separate runs.

2.2.2 Constitutive properties of the bulk PDMS

The constitutive behavior of the PDMS was measured with tensile tests. Tensile specimens were sliced from the cured sheets of PDMS in the dog-bone shape (Figure 2.1 inset). An initial gage length of 18.5 mm was drawn on the specimen, and the specimen was clamped in wedge grips. The tensile tests were performed at a constant displacement rate of 1 mm/sec, and the load was measured using a 250 N load cell. The nominal stress was calculated as the load divided by the original cross-sectional area. A CCD optical camera was used to capture images of the deformed gage length at regular intervals throughout the experiment. These images were used to compute the nominal strains.

A typical nominal stress-strain curve obtained from the PDMS tensile experiments is shown in Figure 2.1. Although the stress-strain curve was sensitive to the curing conditions, it was very reproducible for a given set of conditions. The behavior of the elastomer was non-linear elastic; no hysteresis could be detected upon cyclic loading. Although the curve is non-linear, there is an initial linear portion up to about 30–40%

[1] SPI Supplies, Plasma Prep II

strain. The linear-elastic modulus in this regime was determined to be 3.5 ± 0.2 MPa. The tensile tests were repeated for specimens of the cured PDMS stored for prolonged periods at ambient conditions (in a laboratory, away from direct sunlight) and for specimens of the cured PDMS subjected to the four-minute oxidation treatment. The nominal stress-strain curves for all samples were identical, except for the oxidized samples where there was a slight decrease in the average failure strain from about 80% to about 70%. It is clear that the surface-modified layer was sufficiently limited in its extent that it did not affect the macroscopic properties beyond the slight decrease in failure strain, and the cured PDMS was very stable.

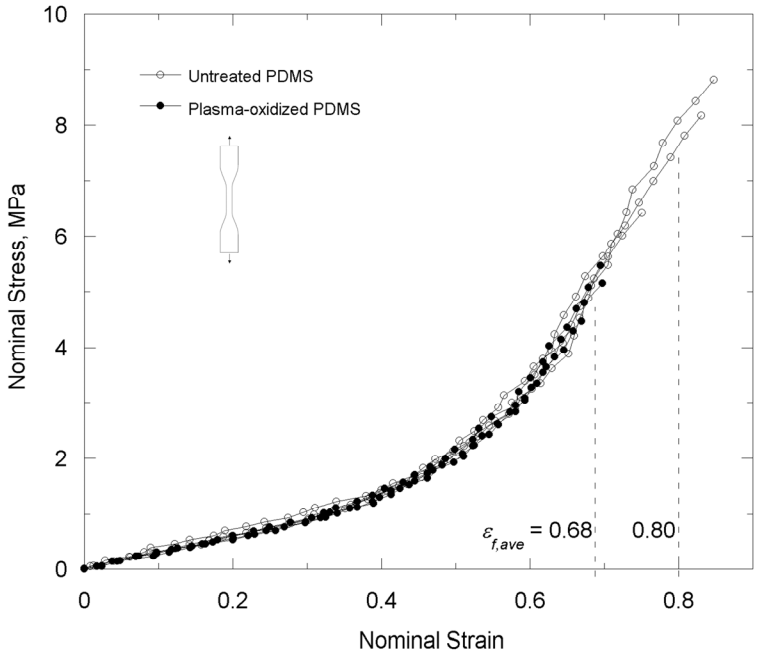

Figure 2.1 – Stress versus strain curves for PDMS
Range of nominal stress versus strain curves obtained from the tensile experiments performed on the bulk PDMS. The strain rate of the samples for the curves shown here was approximately 0.02 s^{-1}; although, it was determined that the PDMS stress-strain behavior demonstrated a negligible dependence on strain rate. The average of the failure strains for the unoxidized (○) and oxidized (●) samples were 80% and 68%, respectively.

2.2.3 Fracture properties of the bulk PDMS

Trouser specimens were sliced from the 2 mm-thick sheets of PDMS with an overall width of 20 mm and initial leg length of 40 mm similar to ASTM Standard D 624–00 (*36*). The surface of the PDMS was scored along the projected crack path with a razor blade to ensure that the crack grew in the center of the legs and fracture remained as a tearing mode, deterred from transitioning to an opening mode. The specimens were loaded at a fixed displacement rate of 1 mm/sec. The load required to tear the PDMS, F_t, was monitored throughout the test and remained constant at 0.3 ± 0.01 N during steady-state crack growth. From this tear load and the thickness, t, of the fractured surface (1.8 ± 0.2 mm), the mode-III toughness was calculated as $\Gamma_{III} = 330 \pm 27$ J/m^2 from the relationship $\Gamma_{III} = 2F_t / t$.

Compact tension specimens were prepared according to ASTM Standard D 5045–99 (*37*) with PDMS that was 6 mm thick (Figure 2.2 inset). Two different methods were used to prepare the specimens. In the first, the compact tension specimens were first cut out of quarter-inch-thick acrylic sheets (Plexiglass®) using a laser cutter[2]. After treating the specimen with a non-stick coating they were placed in a Petri dish and a negative mold was made of them using PDMS. The acrylic specimens were then removed, leaving the PDMS mold. The mold surfaces were treated with a non-stick coating and, finally, the compact-tension specimen were made from the molds. In the second method, two steel thin-walled rods, with an outer diameter of 6.5 mm, were fixed to the bottom of a Petri dish with a center-to-center spacing of 13.2 mm for the pin-grip through-holes (see Figure 2.2 inset). Uncured PDMS was poured into the dish

[2] Universal Laser Systems

to a thickness of 6 mm and subsequently cured. After the PDMS was removed from the Petri dish the compact-tension specimen was sliced out of the PDMS to the appropriate dimensions using a scalpel blade.

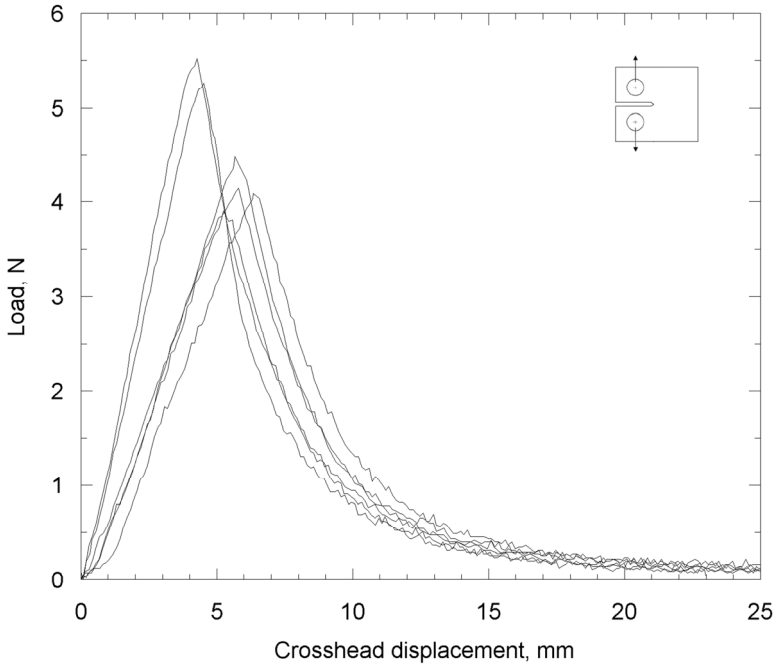

Figure 2.2 – Loading curves from compact tension tests on PDMS
Loading curves from the compact tension tests. A constant displacement rate of 1 mm/s was applied at the pin points to open the crack mouth.

The specimens were loaded at the pin points and a CCD camera was used to monitor the crack growth during the tests. Examples of the resulting load versus displacement curves are shown in Figure 2.2. The difference between the two groupings of loading curves is attributed to the slight variation in the dimensions of the specimen due to the two different specimen preparation methods. The fracture toughness, K_{Ic}, was calculated from the failure load as defined in the standard. The mode-I toughness was then determined to be $\Gamma_I = 238 \pm 50$ J/m^2 from the relationship $\Gamma_I = (1-\nu^2)K_{Ic}^{\ 2} / E$, with $E = 3.5 \pm 0.2$ MPa and $\nu = 0.5$ (as appropriate for an elastomer). These two different methods for obtaining the toughness of the bulk PDMS

appear to be reasonably consistent, and the resulting value will be used as a point of comparison when investigating fracture of the surface-modified layer in a subsequent section of this Chapter.

2.3 Properties of the surface-modified layer

2.3.1 Thickness of the surface-modified layer

Imaging a cross-sectioned piece of oxidized PDMS is the most obvious approach to measure the thickness of the surface-modified layer. However, it was found that sectioning the PDMS by means of a scalpel blade or by fracture – at either ambient or liquid nitrogen temperatures – created a fracture lip at the free surface. This feature was at a similar scale (~0.5 μm) to the expected thickness of the surface-modified layer and dominated any observations made in the scanning electron microscope or atomic-force microscope. It was found that this problem could be eliminated by bonding two slabs of oxidized PDMS and then fracturing the bonded specimen to expose a cross-section containing the interface. An oxidized surface of PDMS readily forms a permanent bond upon contact with another oxidized surface of PDMS, a fact that is exploited in the manufacture of micro-fluidic devices (*38*). However, for the bond to form, at least one of the oxidized surfaces must retain sufficient compliance to achieve good conformal contact. In particular, the surface of PDMS that had been oxidized for four minutes, which was the focus of this study, did not have sufficient compliance. However, oxidation for only one minute appeared to provide the required change in surface chemistry, while retaining sufficient compliance. Therefore, for the purposes of this study, PDMS that had been oxidized for four minutes was bonded to PDMS slabs that had been oxidized for one minute. A crack was then introduced into one of the back

surfaces (perpendicular to the bonded interface), and the specimen was cleaved. The resultant fracture surface was relatively flat, with no delamination or fracture features at the interface.

Imaging a fractured section optically or in an environmental scanning electron microscope produced no contrast between the surface-modified layer and the bulk PDMS used in this study. Methods of surface chemical analysis that have been previously used to study the hydrophobic recovery of plasma-oxidized PDMS (such as X-ray photoelectron spectroscopy, energy dispersive X-ray analysis, or static secondary ion mass spectroscopy (*6, 39*)) did not have the spatial resolution necessary for delineating the region of chemical change on the fractured cross-section. Nor were any topographical features identifiable at the bonded interface using the atomic-force microscope[3] (AFM). However, a clear interface was observed using the phase-imaging function of the AFM in tapping mode. The phase image is a three-dimensional representation of the phase lag between the tapping-mode cantilever's oscillations and the input signal. The phase lag has been shown to depend on the elastic modulus as well as other properties (*e.g.*, visco-elasticity and adhesion) of the material being profiled (*40-43*). Therefore, the fact that a contrast in the phase image at the bonded interface could be seen was taken to be an indication that there was a local change in the material properties at the oxidized surface. The distance over which this contrast could be detected was taken to be a measure of the thickness of the surface-modified layer.

A phase image of the cross-section near the interface region is shown in Figure 2.3a. In this image a clear demarcation can be seen between the PDMS oxidized

---

[3] MultiMode Scanning Probe Microscope, Veeco Instruments, Inc.

for one minute (on the left) and the PDMS oxidized for four minutes (on the right). The phase image did not seem to be very sensitive to any of the minor topographical features captured in a height image of the same region (Figure 2.3b). A line trace on the

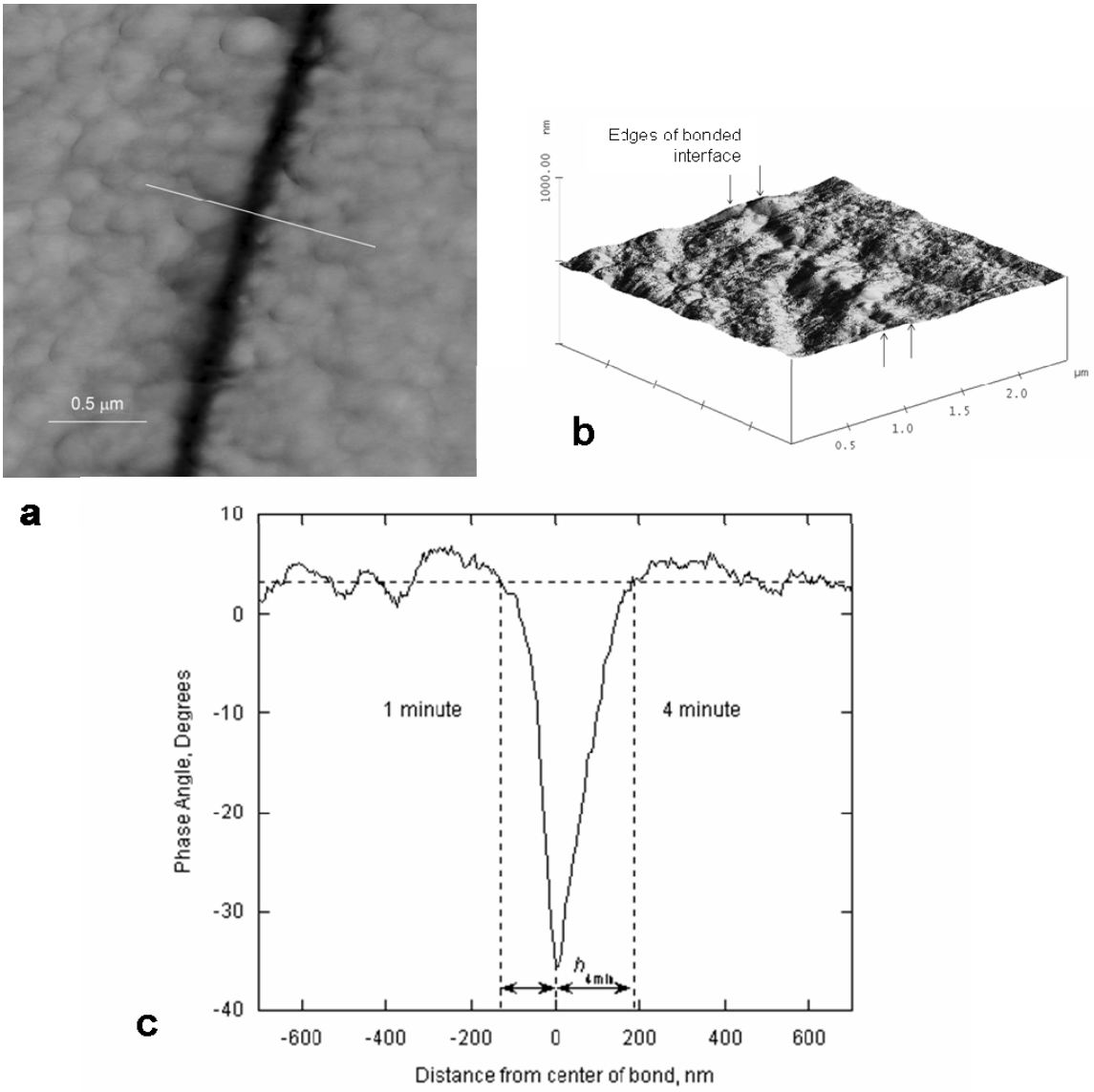

Figure 2.3 – AFM height and phase images of the bonded surface-modified layers
AFM (a) phase and (b) height images of the same region of the cross-section containing the bond between the surface of PDMS oxidized for one minute (on the left) and the surface oxidized for four minutes (on the right). (c) Line trace of the phase angle across the bond at the location of the marker on the phase image in Figure 2.3a. The thickness of the surface-modified layer was measured from the lowest point of the phase angle, at the bond line, to the average value for the bulk material.

phase image across the interface is shown in Figure 2.3c. This trace indicates that any compositional changes within the surface-modified layer were not uniform. The lowest point of the line trace was taken to be the bond line between the two oxidized samples, and the surface-modified layer thickness was measured from this point to where the phase angle returned to the average bulk value (Figure 2.3c). Therefore, the changes are a maximum at the surface and decay to the bulk values over a few hundred nanometers.

The absence of any discontinuity in the phase angle at the interface region in Figure 2.3c indicates that the two surfaces (for the PDMS oxidized for one minute and for the PDMS oxidized for four minutes) may have similar compositions. The only difference between the two oxidation treatments appears to be the thickness of the surface-modified layer. The surface-modified layer for the specimen oxidized for only one minute appeared to be significantly thinner than the layer resulting from oxidation for four times as long, in contrast to reference (*33*). Measurements were taken from two sets of bonded specimens, and multiple traces were taken from each of these specimens. These measurements indicated that the thickness of the surface-modified layer of the specimens oxidized for four minutes was 200 ± 40 nm, with the full range of uncertainty being exhibited in a single specimen. The measurements also indicated that the thickness of the surface-modified layer in a specimen oxidized for one minute was approximately half as thick as a layer resulting from four minutes of oxidation. An associated set of experiments was performed in which one half was oxidized for one minute and the other was oxidized for one minute, 20 minutes, 40 minutes, and 60 minutes. It was confirmed that the one minute of oxidation indeed resulted in a surface-

modified layer thickness of 110–125 nm (*44*) and the rest of the oxidation times resulted in layer thicknesses of 380 ± 40 nm, 460 ± 40 nm, and 730 ± 45 nm, respectively (Figure 2.4). Although not exact, these results are suggestive of a diffusion-dominated oxidation process where the depth is predicted to be proportional to the square-root of the time of exposure (Figure 2.4). In fact, the relationship between the phase angle and

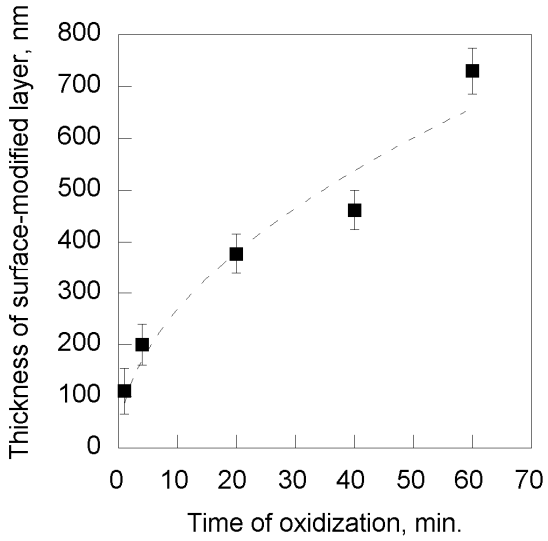

Figure 2.4 – Thickness of the surface-modified layer versus time of oxidation
The relationship between the time of oxidation and the resulting thickness of the surface-modified layer measured using the AFM phase-imaging method. The dashed line is an approximate fit to the data of the form: $h = C\sqrt{t}$.

the distance from the presumed interface on the four-minute side shown in Figure 2.3c is not inconsistent with an error function that would be the expected result from a diffusion-dominated process; although, the data does not allow the issue to be resolved unambiguously. From this data, it is clear that the surface-modified layer thickness must increase with increasing time of exposure to oxygen plasma, in contrast to the results of Hillborg, *et al.*, 2000 (*33*). Therefore, for the purposes of the subsequent analyses, an approximation was made that the properties of the surface-modified layer

followed a linear profile – a more meaningful approximation than that of a discrete layer.

2.3.2 Elastic modulus of the surface-modified layer

Nanoindentation was performed using the "force mode" of the AFM. Before each set of indents was performed, the cantilever deflection was calibrated by bringing the probe into contact with silicon, which provided a hard reference surface. The first set of experiments involved the use of a relatively stiff AFM probe (with a cantilever stiffness of k = 40 N/m, as determined by the manufacturer[4]) to indent oxidized PDMS. Figure 2.5 shows that the resultant plot of load against indentation depth is reminiscent of a characteristic plastic indent (*45*). The indentation depth reached between 2 and 3 μm, and subsequent imaging in the AFM revealed a puncture in the surface-modified layer measuring about 1 μm in width and 50 nm in depth. However, rather than trying to extract any information about the surface-modified layer from this type of behavior, the effect of using a more compliant cantilever was explored.

[4] Veeco Probes, Inc.

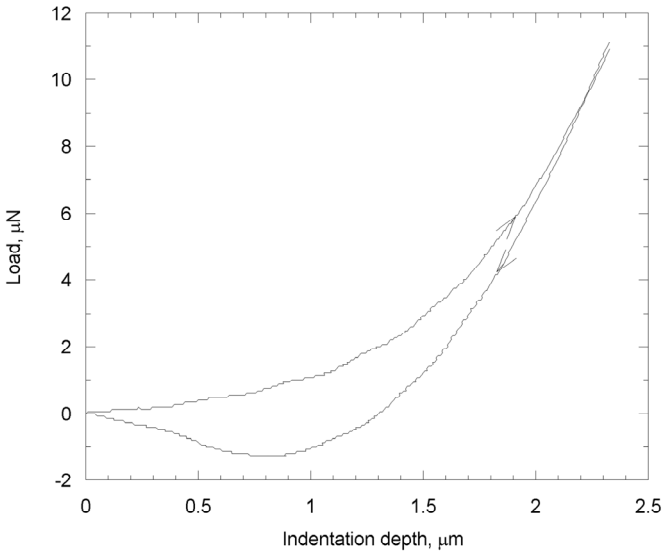

Figure 2.5 – Indentation curve for surface-modified PDMS, *k* = 40 N/m
Load versus indentation depth curve for the stiff cantilever (*k* = 40 N/m) indenting on the surface-modified layer of PDMS. The indentation depth was greater than ten times the measured thickness of the surface-modified layer and the shape of the curve is reminiscent of a characteristic plastic indent.

Qualitatively different indentation curves were obtained when a relatively compliant cantilever (*k* = 0.58 N/m) was used to indent unoxidized and oxidized PDMS surfaces. Indentation on an unoxidized PDMS surface showed the classical non-linear behavior (with essentially no hysteresis) associated with the contact mechanics of elastic indentation (Figure 2.6). No permanent indentation impression was found during subsequent imaging by AFM. In contrast, indentation on an oxidized PDMS surface resulted in a linear relationship between the cantilever deflection and the translation of the sample, with some evidence of adhesive contact as the AFM probe came into contact with and left the surface (Figure 2.7). Multiple indentations were performed on a single sample of PDMS that had been oxidized for four minutes, with recalibration repeated during the experiment. All the indentations were very consistent and resulted in a characteristic plot of load against indentation depth shown in Figure 2.8.

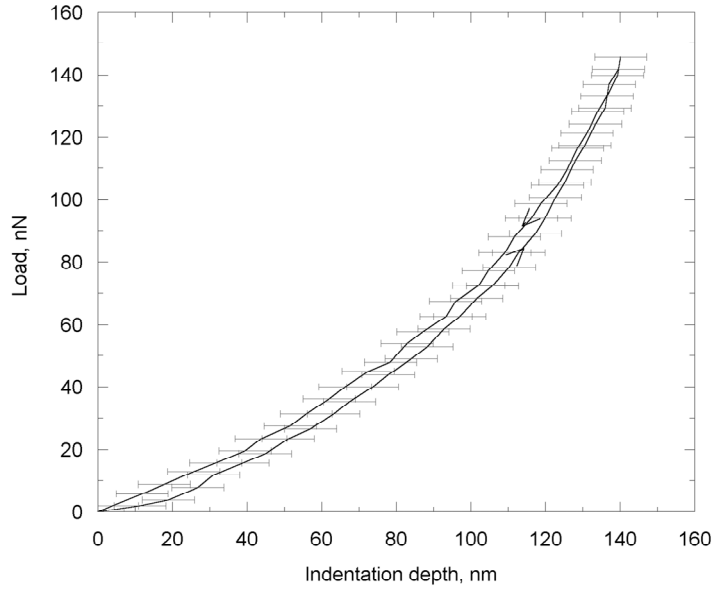

Figure 2.6 – Indentation curve for unmodified PDMS, *k* = 0.58 N/m
The load versus indentation relationship for the compliant cantilever (*k* = 0.58 N/m) indenting on unoxidized PDMS showed typical contact mechanics of elastic indentation with no apparent hysteresis between the indentation and retraction portions of the curve. Subsequent imaging did not reveal any permanent damage on the unmodified surface of the PDMS.

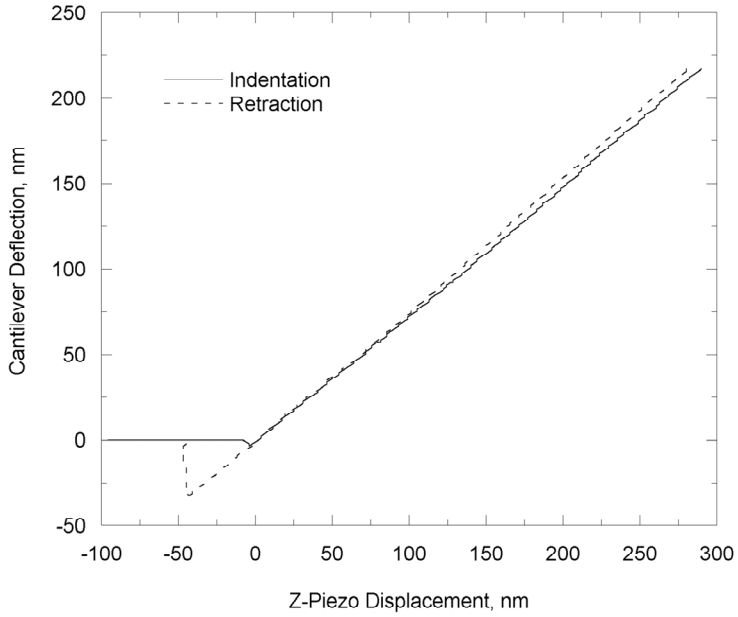

Figure 2.7 – Indentation curve for surface-modified PDMS, k = 0.58 N/m
The cantilever deflection (directly related to load) versus z-piezo displacement (directly related to indentation depth) relationship for the compliant cantilever (*k* = 0.58 N/m) indenting on oxidized PDMS is linear as shown by this example of the relationship between cantilever deflection and z-piezo travel distance. The indentation curve is the solid and the retraction curve is the dashed line.

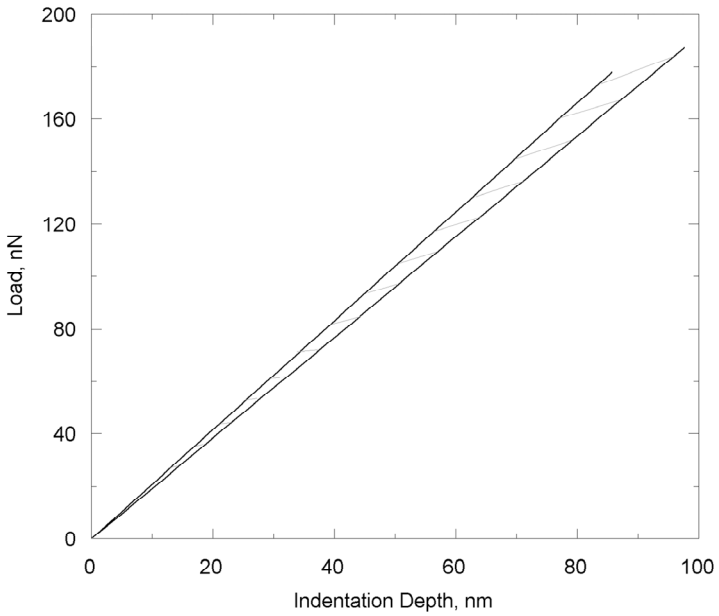

Figure 2.8 – Range of linear indentation curves for surface-modified PDMS
The range of load versus indentation depth curves for all indents taken in various positions on the surface-modified layer of one PDMS sample that had been oxidized for four minutes.

This linear relationship between load and indentation depth for the oxidized PDMS (Figure 2.8) indicates that the contact area between the probe tip and the material did not increase with indentation depth, as would be expected from classical indentation models. Instead, the behavior is consistent with point loading of an elastic beam on an elastic foundation. It is this model that can be used to extract the properties of the surface-modified layer. The deflection, Δz_i, of an elastic plate bonded to an elastic half-space and subjected to a point load, P, is given by (*46*)

$$\Delta z_i = \frac{P}{3\sqrt{3}}\left(\frac{(1+\nu_s)^2(3-4\nu_s)}{4E_s^2(1-\nu_s)^2 D}\right)^{1/3}, \qquad (1)$$

where D is the bending stiffness of the plate, E_s is the modulus of the substrate and ν_s is the Poisson's ratio of the substrate. As discussed in Section 2, E_s for this material is

3.5 ± 0.2 MPa, and ν_s can be taken to be equal to 0.5. Therefore, the relationship between the indentation depth and applied load is given by

$$\frac{P}{\Delta z_i} = 9.1(\pm 0.3) \times 10^4 D^{1/3} \qquad \text{N/m.} \tag{2}$$

From Figure 2.8, it can be seen that the experimental relationship between the load and indentation depth is in the range of 1.9 to 2.1 N/m. Therefore, a comparison with Eqn. 2 indicates that the bending stiffness of the surface layer is equal to (1.1 ± 0.2) x 10^{-14} N·m.

To estimate the modulus from a bending stiffness requires knowledge of the thickness and whether the modulus varies through the thickness of the surface-modified layer. As discussed in Section 3.1, it is assumed for the purposes of analysis that the modulus decreases linearly from a value designated as E_f at the surface to E_s at the depth previously identified as the thickness of the surface-modified layer, h. With this linear assumption, the bending stiffness of the surface layer can be calculated as

$$D = \frac{\left(\overline{E}_f^{\,2} + 4\overline{E}_f \overline{E}_s + \overline{E}_s^{\,2}\right)h^3}{36(\overline{E}_f + \overline{E}_s)}. \tag{3}$$

Here, $\bar{E}_f$ and $\bar{E}_s$ refer to the plane-strain moduli of the surface-modified layer and PDMS, respectively. Substituting into this equation the values h = 200 ± 40 nm, E_s = 3.5 ± 0.2 MPa, ν_s = 0.5, and D = (1.1 ± 0.2) x 10^{-14} N·m results in a value for the surface modulus of $\bar{E}_f$ = 37 ± 10 MPa. This maximum value of the modulus at the surface of the oxidized layer is between 7 and 13 times larger than the modulus of the substrate. If it were to be assumed that the properties of the surface-modified layer

were not graded, but were uniform over a thickness of about 200 nm, then the effective modulus of the layer would be 12 ± 3 MPa from the relationship $D = Eh^3/12(1-\nu^2)$.

In the experiments described in the following section, buckling of the surface layer was observed. The details of this observation can be used as a point of comparison for the results presented above. For a uniform plate of thickness *h*, the buckling wavelength of a surface layer is expected to be of the form (*47, 48*)

$$\lambda = 9.97\left(D\left(1-\nu^2\right)/E_s\right)^{1/3}. \tag{4}$$

From this equation and the values of bending stiffness, *D*, and substrate modulus, E_s, determined in the present study, the predicted buckling wavelength would be about 1.3 μm. Not taking into account the effect of a graded layer on the buckling wavelength (studies presently underway (*49*)), this computed buckling wavelength is very close to the experimentally observed wavelength which was found to be 1.34 ± 0.06 μm and provides some confirmation of the magnitude of the properties of the surface-modified layer.

2.4 Fracture of the surface-modified layer

2.4.1 Experimental observations

Once the properties of the surface-modified layer have been determined, observations of the nano-cracking behavior can be compared to mechanics models. A controlled experiment was performed in order to study the behavior of the nano-cracking with respect to applied tensile strain. Several PDMS specimens were oxidized for four minutes in the same run in order to ensure that the surface-modified layer on each was as close to the same as possible. After oxidation, some of these specimens

were used to determine the resulting thickness and modulus of the surface-modified layer (as reported in the previous sections). The remaining rectangular pieces (40 mm x 10 mm x 2 mm) were individually mounted in a manual micrometer-screw-driven tensile machine[5] and strained in tension. These specimens were organized into five sets of two specimens, and each set was tested to different levels of nominal strain: 6, 10, 15, 20, and 30%. One specimen from each set was removed from the testing machine and relaxed before being examined. The other specimen from each set was left in place under an applied strain while a PDMS replica was created of its surface. To ensure complete removal of the replica the cracked surface was first exposed to a silane treatment[6] to increase the hydrophobicity of the surface-modified PDMS. Molds of the surfaces of the specimen under applied strain were necessary because the configuration of the optical head of the AFM used for these studies prevented *in situ* stretching of the samples. Square sections of approximately 10 mm by 10 mm were then cut from the center region (away from the ends gripped by the stretcher) of both the relaxed specimens and the replicas of the strained surfaces. The surfaces of both sets of specimens were imaged using the AFM in tapping mode.

---

[5] MicroVice Holder (S.T. Japan USA, LLC. FL, USA)

[6] For seven minutes in a vacuum chamber a 1:1 mixture of (tridecafluoro-1,1,2,2-tetrahydrooctyl)-1-trichlorosilane and mineral oil was evaporated onto the cracked surface to form a monolayer of silane molecules.

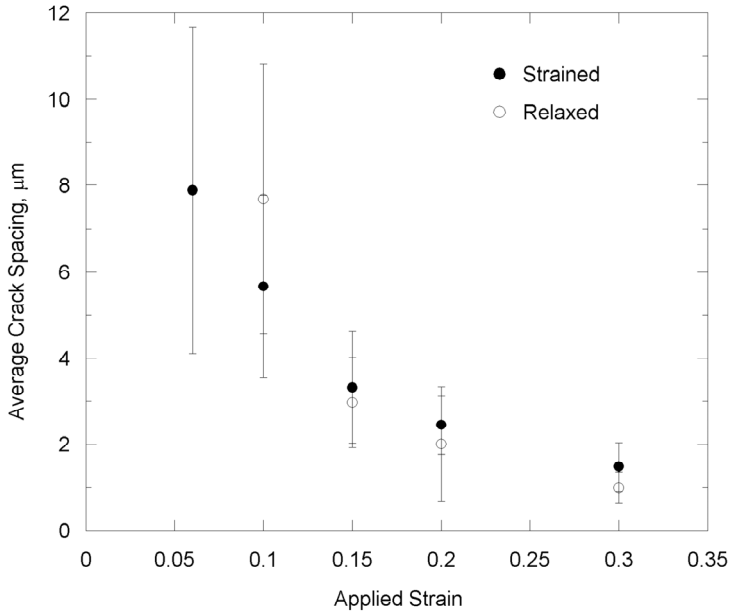

Figure 2.9 – Average crack spacing versus applied strain
Average crack spacing versus applied strain. Data taken from molds made of strained specimens are indicated by solid circles (●). Data taken from direct measurements of relaxed specimens are indicated by open circles (○).

The applied tensile strain resulted in a series of parallel nano-cracks in the surface-modified layer oriented perpendicular to the direction of stretching. The average crack spacing was measured from a series of AFM images and is plotted as a function of the applied strain for all the specimens in Figure 2.9. Consistent with prior analyses and observations of thin-film cracking (*10-12*), the average crack spacing decreased with increasing applied strain. In addition to the nano-cracks, for tensile strains of 15% and above, surface buckles were induced perpendicular to the cracks with a wavelength of 1.34 ± 0.06 µm. An image taken with the AFM of a surface that has been cracked by an applied strain and then allowed to relax is shown in Figure 2.10; while an image taken from a replica of a strained surface with the accompanying surface buckling is shown in Figure 2.11.

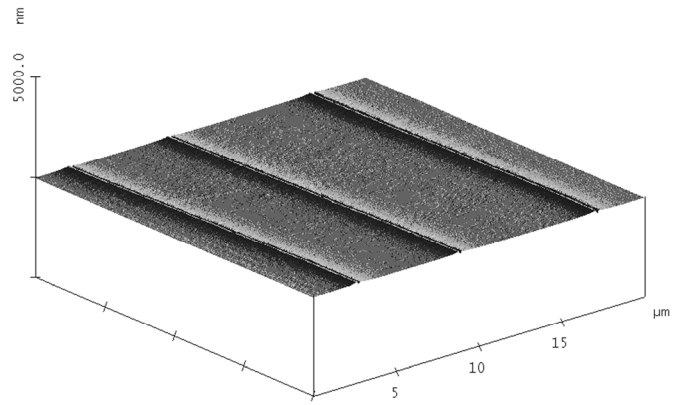

Figure 2.10 – AFM height image of nano-cracks (relaxed)
AFM image of the relaxed nano-cracks introduced into the surface-modified layer of PDMS by the application of a 10% applied tensile strain.

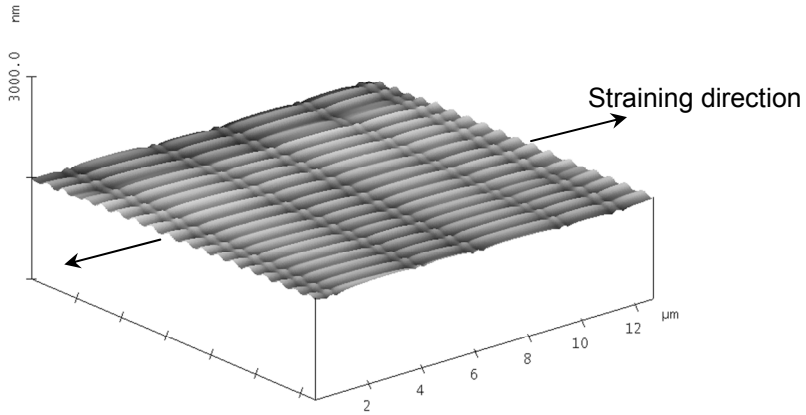

Figure 2.11 – AFM height image of nano-cracks (strained)
AFM image of the PDMS mold of strained nano-cracks with the accompanying surface buckling. These nano-cracks were created by the application of 15% applied tensile strain in the direction perpendicular to the cracks.

The buckles created by the application of the tensile strain seem to be created by a different mechanism than those created by an imposed compressive strain (*31*). The surface buckles are always observed to occur at strains greater than those that introduce the nano-cracks. Therefore, it is presumed that they are associated with the development of the nano-cracks, and it is postulated that they form by the following mechanism. The cracks cause stress relaxation in the material between them. The material below the cracks supports a tensile strain in the axial direction. Poisson's ratio

effects induce a lateral contraction in the material below the cracks, which imposes a lateral compressive stress on the material between the cracks. This compressive stress, in conjunction with the modulus mismatch between the surface layer and the bulk, results in surface buckles. The mechanics of the surface buckling for this geometry is being addressed elsewhere (*49*).

The profiles of individual nano-cracks (or replicas of nano-cracks) were examined in detail by AFM; an example of a typical profile is shown in Figure 2.12. It may be noted that the shape of the crack shown in Figure 2.12 has some resemblance to the shape of cracks formed by surface diffusion (*50, 51*), where the rise near the crack

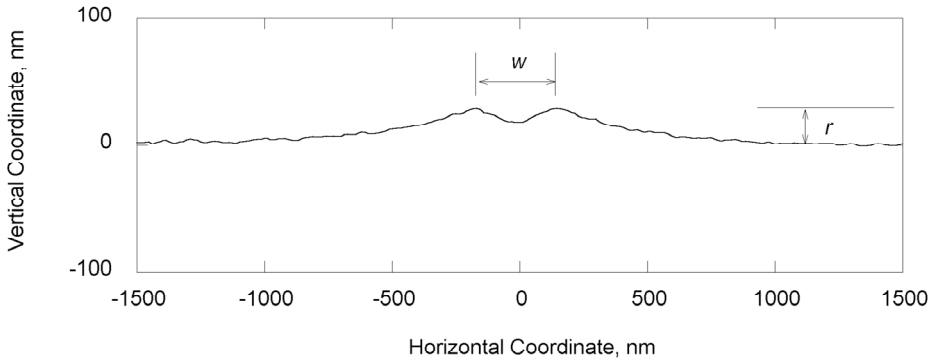

Figure 2.12 – Profile of a nano-crack obtained with the AFM
A typical profile of a nano-crack obtained with the AFM. This particular profile has been vertically reversed from the data taken from a mold of a specimen strained to 10%. The width, *w*, and rise, *r*, of the cracks were measured as indicated.

mouth is associated with effects of surface diffusion. However, the role of diffusion in the formation of the cracks was eliminated by a series of studies where the relaxed crack profile was continually monitored by AFM for a period of eight hours after being created. Insignificantly small changes were observed in the crack geometry, leading to the conclusion that all effects discussed in this Chapter are dominated by elasticity.

Therefore, the rise must be associated with the effects of Poisson's ratio at the crack surface. Since the crack surface relaxes in-plane strains, the out-of-plane contractions must also relax, causing the surface near the cracks to rise. The relatively smooth curves at the crack mouth were not expected for an elastic crack; this feature may be associated partly with the geometry of the AFM tip. They may also be associated with the effects of surface tension deforming the relatively compliant material (*22*).

The cracks were characterized by three parameters: the crack spacing (the average distance to the nearest two neighbors), L; the crack opening, w; and the maximum height that the edges of the crack rise above the surface of the PDMS, r. The crack rise and opening are exterior features of the crack and could be determined with reasonable accuracy by AFM imaging of either the relaxed specimens or the replicas. The widths of the cracks are plotted as a function of the average distance to their nearest-neighbor cracks in Figure 2.13a. The corresponding rises of the cracks are plotted as a function of the average distance to the nearest-neighbor cracks in Figure 2.13b.

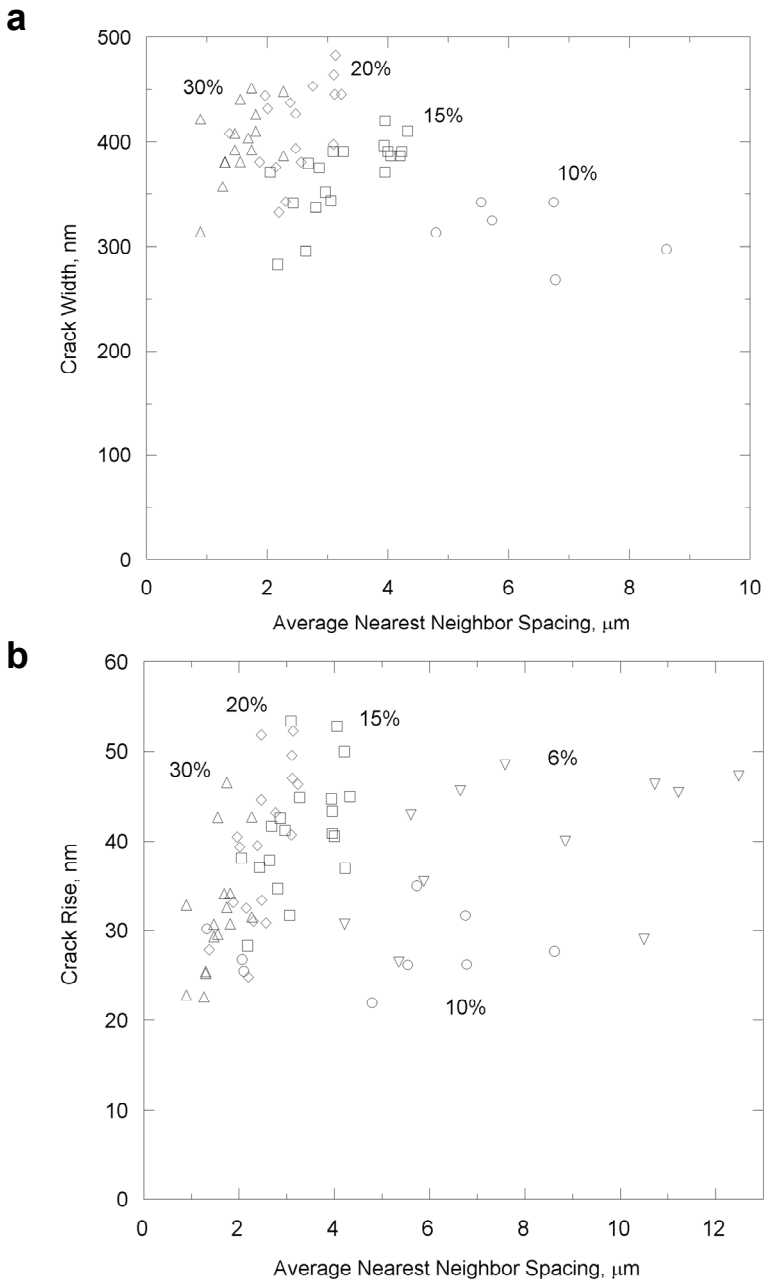

Figure 2.13 – Nanocrack width and rise versus crack spacing
(a) Crack widths, *w*, and (b) crack rises, *r*, were experimentally measured when possible from the molds of strained specimen and are plotted against the average nearest neighbor crack spacing, *L*, for 6% (∇), 10% (○),15% (□), 20% (◊), and 30% (Δ) applied strain.

The crack depth, *d*, could not be determined directly since the AFM probe could not penetrate to the tip of the crack, nor was there any guarantee that the PDMS used to make replicas of the cracked surface could flow all the way to the crack tip. Other experimental procedures were attempted in order to obtain a direct measurement of the

crack depth. Sectioning (by fracture) a cracked slab of PDMS resulted in damage to the free edge of the specimen, so that attempts to image the cracked edge or a replica of the cracked edge with the AFM were unsuccessful. Bonding a cracked specimen to another oxidized piece of PDMS (in a manner similar to that discussed in Section 2.3.1) failed because the surface topography introduced by the cracks prevented intimate contact between the two surfaces. Finally, two slabs of oxidized PDMS were bonded together, sectioned, and then strained after bonding. This resulted in the appearance of cracks on a replica of the strained cross-section containing the bond. However, even here, it was not possible to make an accurate measurement of the crack depth. Estimates of the crack depth were eventually made by comparison to the results of finite-element calculations, as demonstrated in the following section.

2.4.2 Discussion

2.4.2.1 Effects of possible residual strain

The morphology of the nano-cracks in the relaxed specimens took two different forms. In one, the cracks were simply narrower, shorter versions of the strained cracks, with measurable widths and rises (Figure 2.10). In the other, the cracks appeared to have completely but imperfectly healed, leaving the appearance of an overlapped edge (Figure 2.14). The net density of the open and healed cracks on the relaxed specimens was comparable to the density of the cracks measured from the replicas taken from the corresponding strained specimens. This indicates that the origin of both types of cracks is the same—they are formed during tensile loading. The existence of open cracks after the load is removed indicates, in the absence of any obvious hysteresis effects, that there must be a residual tensile stress introduced by the oxidation process in the surface-

modified layer. The morphology of the healed relaxed cracks (Figure 2.14) indicates the following further understanding of the mechanics of crack closure. While the small residual tensile stress associated with the oxidation process is often sufficient to hold open many of the cracks generated, the cracks are at a scale where they are on the border between remaining open because of the residual tension and spontaneously collapsing under the effect of surface forces. If a crack does collapse, the tension perpendicular to the crack surfaces that is associated with the surface forces induces a lateral compressive strain parallel to the crack. This local compression in conjunction with the modulus mismatch between the surface-modified layer and the substrate leads to the buckling pattern observed in Figure 2.14. This understanding is supported by the observation that the period of the buckles in Figure 2.14 is similar to that of the surface waves observed upon applying a tensile load to the cracked specimens.

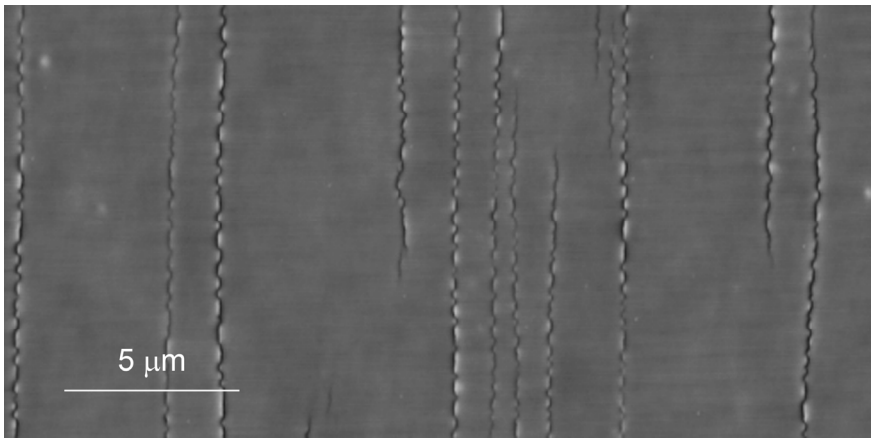

Figure 2.14 – Surface morphology of healed nano-cracks
In this AFM height image of the surface of a specimen that had been relaxed from 20% applied tensile strain the relaxed cracks have taken the healed morphology. The cracks collapse due to surface forces acting on the crack faces. Tension induced at the edges of the cracks causes the appearance of buckling. The wavelength of the buckled edge is consistent with the buckling wavelength on the molds of the strained cracks.

In conclusion, the observations on the relaxed specimens indicate that the oxidation process induces a small tensile strain. The residual strain must have been

relatively small after this four-minute oxidation, because it was insufficient to prevent many of the cracks from collapsing. Therefore, the effects of any residual stress induced by the four minutes of oxidation are neglected in the analyses that follow. However, it was noted that specimens oxidized for a significantly longer period of time tended to form spontaneous cracks without the need to apply a tensile load. This is consistent with the notion that the increased oxidation time results in a thicker surface-modified layer or/and increased tensile strain.

2.4.2.2 Effects of elapsed time on crack patterns

After oxidization, the newly-formed hydrophobic surface state is not stable for a very long period of time and it regains its original hydrophobic state within a matter of several hours. This phenomenon in PDMS has been studied extensively (*2, 3, 33*) and is termed hydrophobic recovery. The most advanced and accepted explanation for hydrophobic recovery is that low molar mass species migrate from the bulk PDMS to the surface after oxidization (*33*). This process is presumed to be expedited by the presence of cracks in the surface-modified layer. There is some evidence that the complete effects of the change that takes place in the surface of PDMS upon oxidization are not lost, as its hydrophilicity is. In one study, for example, cells adhered to PDMS only after it had been oxidized, regardless of the time that had elapsed since the exposure to plasma oxygen and whether its surface state remained hydrophilic or not (*52*). Furthermore, a study of the relative stiffness of the surface of PDMS with time after plasma oxygen exposure showed that there was not a significant drop in the surface stiffness that accompanied the hydrophobic recovery (*4*).

With the ambiguity surrounding the dynamic nature of the surface-modified layer on PDMS after exposure to plasma oxygen it is natural to wonder whether the crack patterns are stable and permanent in the surface or whether they are altered or removed along with the hydrophobic recovery. To address this concern, an experiment was performed where a slab of PDMS was oxidized for four minutes then it was strained to produce cracks. A sample was trimmed from the slab for analysis with the AFM. The first surface profile was taken 20 minutes after oxidization. The sample was left in place on the AFM scanner and subsequent images were captured at 50 minutes, 90 minutes, and 10 hours after oxidization (Figure 2.15). Some drift in the piezo scanner was apparent. However, over the range of time of the experiment there did not appear to be a significant change in the dimensions of the crack that was monitored. The width

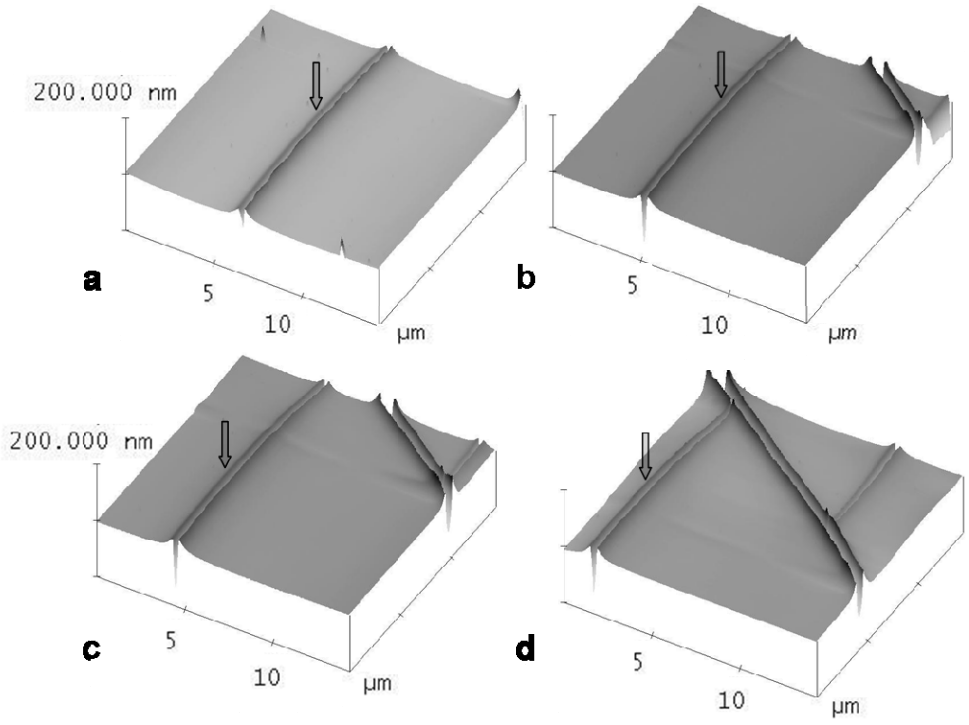

Figure 2.15 – Nanocrack shape with time
A series of images taken with the AFM at (a) 20 minutes, (b) 50 minutes, (c) 90 minutes, and (d) 10 hours after oxidization (and stretching) of a slab of PDMS. Although there is significant drift in the piezo scanner, the size of the monitored crack (marked with an arrow in each image) did not change with time after exposure to oxygen plasma.

did not change; although, between 20 and 50 minutes there was an increase of the measured depth of the crack (Figure 2.16). Over the course of this study oxidized and cracked PDMS samples have been allowed to rest in ambient conditions and then AFM profiles of the cracked surface were taken after time periods of up to a month. The surfaces still contained cracks on the order of what was measured directly after fabrication of the specimen.

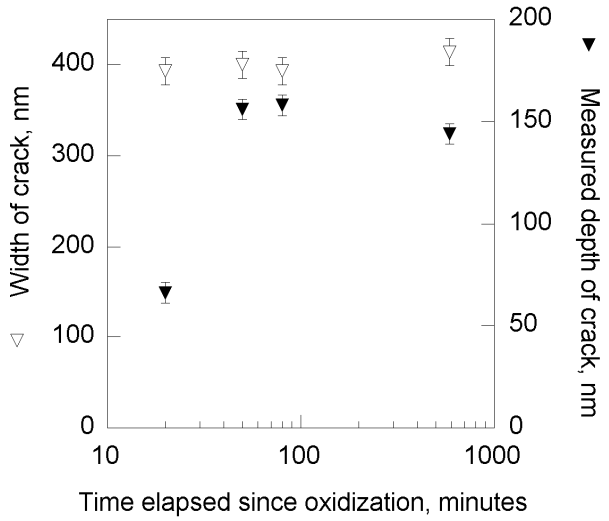

Figure 2.16 – Nanocrack width and depth versus time
The average width and depth of the monitored crack were measured from the AFM profiles taken at various time intervals after oxidization.

2.4.2.3 Crack depth

In the absence of any residual strain, both the width, w, and the rise, r, of the cracks are dependent only on the properties of the system— $\overline{E}_s$, $\overline{E}_f$, and h—and on the crack spacing, L; depth, d; and applied strain, ε_{app}. Since the specimens used to produce the plots of Figure 2.13 were all oxidized at the same time, E_f and h are expected to be reasonably constant for all the data points shown. Therefore, the large variability seen for the data taken from the strained cracks at equal values of ε_{app} and L indicates a

substantial variability in crack depth. It is likely that the variability in crack depth is associated with the fact that the interface between the surface-modified layer and the bulk material was not smooth (Figure 2.3a).

Estimates of the crack depths were made using finite-element calculations of particular cracked geometries and the measured properties of the PDMS and surface-modified layer. An example of the appropriate model and mesh for a single crack is shown in Figure 2.17. In general, the calculations should be done with asymmetrical boundary conditions, reflecting the non-uniform crack spacing. But, effects of this asymmetry were small compared with other experimental variables and were ignored. Therefore, periodic boundary conditions were used, with the lateral extent of the model being set to the average $L/2$ for the particular crack being modeled. The bulk PDMS was modeled with 2D plane-strain hybrid elements and its material behavior was modeled as hyperelastic. The experimentally determined stress/strain curve (Figure 2.1) was used to define the constitutive properties. The graded surface-modified layer was modeled with 2D plane-strain linear-elastic elements; its modulus was varied from 37 MPa on the surface to 3.5 MPa at a distance of 200 nm from the surface. A displacement boundary condition was used to simulate the applied strain. The resulting width and rise of the crack were determined from the numerical output, using the same definitions as in the experiments. A series of numerical calculations was conducted with different crack depths, but keeping the crack spacing and strain corresponding to one particular set of experimental results. By comparing the numerical results for the rise and width to the experimental values, an estimate of the actual crack depth could be

obtained. This process of comparison was repeated for a number of different sets of applied strain and crack spacing.

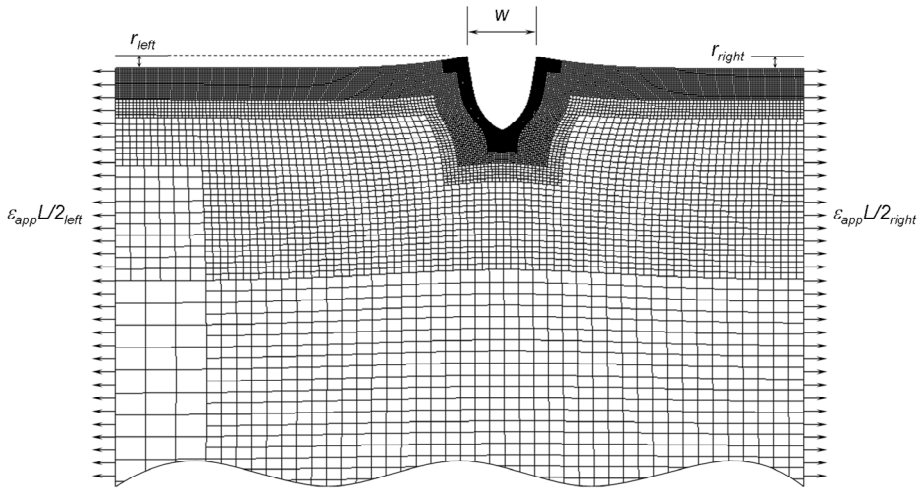

Figure 2.17 – Finite-element mesh for nanocrack studies
Finite-element mesh used for fitting the width and rise of the cracks to both find the depth of penetration of the cracks and to estimate the average toughness of the surface-modified layer. The lateral dimension on either side of the crack is *L/2* for the appropriate crack spacing being modeled. The crack depth can be fixed to anywhere in the region marked d_o. Using the average spacing approach, only half of the crack is modeled and the appropriate periodic boundary condition is applied at the plane corresponding to the crack face.

The limited range of possible fits between the numerical results and the experimental observations indicated that the cracks had to extend beyond the thickness previously deduced for the surface-modified layer. The calculated crack depths were in the range of about 300 to 600 nm irrespective of the level of applied strain, compared to a thickness of about 200 nm for the surface-modified layer. The fact that the oxidation process may be affecting the toughness of the PDMS to depths from 150% to 300% greater than the depth to where the modulus is affected has significance for the observations of the crack spacing. If the cracks are extending well below the high-modulus region, then the crack spacing can be modeled by results for an elastically homogeneous system (*11, 12*). In other words, one would expect the crack spacing to be of the order of a few multiples of the crack depth—not vastly more as would be

expected for a cracked stiff layer on a compliant substrate (*10*). The magnitudes of the crack spacing are not inconsistent with this conjecture.

2.4.2.4 Toughness of the surface-modified layer

The average toughness of the surface-modified layer, over a thickness corresponding to the depth of the cracks, was estimated by computing the energy-release rate of a tunneling crack. As the applied strain was increased during the tensile tests, cracks tunneled at increasing densities. A new crack can propagate between two existing cracks only if the energy-release rate for tunneling exceeds the toughness of the surface-modified layer. The stochastic nature of the distribution of the cracks and the absence of *in-situ* monitoring of the formation of the cracks results in an ambiguity in deducing the appropriate crack spacing at which to carry out analyses. Therefore, two different approaches were explored in this study. In one, the minimum average distance to the nearest neighbors found for any crack at a given level of strain was used as the spacing at which a crack could just be propagated at that strain. In the other, this critical spacing was assumed to be given by the smallest nearest-neighbor spacing found at a given strain level. The results from both approaches were comparable.

The calculations were conducted by calculating the change in the total elastic energy between the cracked and uncracked geometry (Figure 2.17). Periodic boundary conditions, suitable to each of the two different approaches, were used with applied displacements corresponding to the appropriate applied strain. The calculations were done for a range of crack depths, corresponding to those deduced earlier. The strain energy (per unit width) of the uncracked configuration was calculated, and then the strain energy (per unit width) of the cracked configuration was calculated. The energy-

release rate for tunneling was found by dividing the change in energy by the crack depth. Since the energy-release rate was calculated for the extreme conditions under which cracks tunneled, this energy-release rate was directly equated to the toughness. The results of the calculations were insensitive to the particular approach used to choose the minimum crack spacing and produced an estimate of the toughness in the range of 100 to 300 mJ/m^2. This remarkably low toughness—a drop by three orders of magnitude from the bulk value for the PDMS of about 250–300 J/m^2—indicates a significant embrittling of the surface layer by the oxidation. Chaudhury and Whitesides (*53*) estimated the free surface energy, γ_s, of plasma-oxidized PDMS to be approximately 60 mJ/m^2. Therefore, the calculated toughness range is very close to $2\gamma_s$, which indicates that the surface-modified layer is almost perfectly brittle. This is in contrast to the relatively high toughness of the bulk PDMS, which indicates some crack-tip dissipative mechanisms, probably pull out of the molecular chains.

2.5 Concluding remarks

A relatively quick and simple method has been demonstrated for determining the thickness and elastic modulus of the surface-modified layer created on PDMS by exposure to plasma oxygen. This method takes advantage of a substantial modulus mismatch between the stiff surface-modified layer and the compliant substrate to interpret the results of two different AFM probing techniques. The first uses the phase shift in the tapping-mode cantilever vibration when passing over the two different regions on the cross-section of oxidized PDMS to measure the thickness of the surface-modified layer. The second utilizes the solution of plate bending on an elastic foundation under a point load exerted by the AFM probe to deduce the elastic modulus

of the surface-modified layer. Using these methods, a surface-modified layer created by four minutes of exposure to oxygen plasma was determined to have a modulus varying from about 37 MPa at the surface to a bulk value of 3.5 MPa at a depth of about 200 nm below the surface.

An array of parallel nano-cracks is produced within the surface-modified layer upon the application of a uniaxial tensile strain. The crack spacing decreased with increased applied uniaxial tensile strain as expected from existing analyses of cracking in thin films. While the depth of the cracks could not be determined directly, it could be estimated by comparing experimental observations of the crack opening, surface rise, and spacing with finite-element calculations for these quantities using the measured properties of the surface layer. These estimates indicated that there was a stochastic variation in the crack depth, without any systematic effect of applied strain. The surface layer was essentially perfectly brittle with a calculated toughness of about 100–300 mJ/m^2 to a depth of about 300–600 nm below the surface. The lower bound of this toughness is about twice the reported free surface energy of oxidized PDMS. Finally, it was noted that the oxidation process produced a very small level of residual tensile stress; however, this was too small to prevent the majority of the cracks from collapsing upon unloading.

Chapter 3

Fracture patterning of surface-modified PDMS cubes and microspheres

3.1 Introduction

The controlled fabrication of two- and three-dimensionally (2D and 3D) ordered structures is important for the micro/nano-engineering of materials and devices. (*54-56*) One of the most accessible and useful technologies for laboratory micro/nanofabrication is the set of methods commonly referred to as soft lithography where patterning is performed using structures constructed on an elastomeric polymer, typically polydimethylsiloxane (PDMS). Microcontact printing (μCP), for example, is a versatile soft lithographic technique in which molecular patterns are transferred to flat (*57*), smoothly curved (*58*), or spherical (*59*) surfaces using PDMS stamps. Additionally, a combination of chemical vapor deposition (CVD) and projection lithography can be used to produce colloids (100 μm< ϕ < 400 μm) with high-precision surface structures (*60*). Although versatile, these techniques are often not effective for generation of patterns on the order of a micron or smaller on small three-dimensional objects.

Patterned three-dimensional micro- to nano-scale particles can be used as building blocks for self-assembled structures. The resultant assembly is driven by the size and shape of the particle as well as the surface patterning on the particles (*14, 15*)

which is challenging when the surface is not flat. Several methods have been developed to pattern the surfaces of particles. One of these is the stamping of a monolayer of particles which capped the particles with a film of opposite charge (*59*). Application of a resist via chemical vapor deposition rather than the more typical spin-on resist is another way of side-stepping techniques generally only available for flat surfaces (*60*). Particles can be released from a sacrificial mold after having been patterned on one exposed surface using typical lithography methods. This technique has been used to cap microspheres with gold and subsequently functionalize with DNA strands (*61*).

In Chapter 2, a method for fabricating a nano-scale pattern over a large area of material was discussed. In this method, PDMS-supported brittle thin films were subject to an externally applied tensile strain which induced fracture of the layer generating parallel nano-scale cracks over large (1 cm^2 or larger) flat substrates (*1, 62*). In this Chapter, a variation of this method is described where crack patterns are formed by external compression rather than stretching. This compression-based method has the advantage of being able to create patterns on small objects where direct stretching would be very difficult. The crack patterns produced by this method are characterized using two representative objects: cubes with dimensions of approximately 2 mm and microspheres with diameters ranging from 200 μm to 800 μm.

3.2 Experimental

3.2.1 Materials preparation

Polydimethylsiloxane prepolymer (Sylgard 184, Dow Corning) was prepared by mixing the curing agent and polymer base in a weight ratio of 1:10. The pre-polymer for the cubes was poured into Petri dishes to a thickness of approximately 2 mm and was

then cured in an oven at 60°C for 24 hours. After curing, the 2 mm-thick sheet was manually cut into cubes. The pre-polymer for the microspheres was placed in a glass bottle in a weight ratio of 1:10 with DI water containing 0.1 wt% Pluronic F108[1]. The container was vibrated for approximately 5 to 10 seconds with a vortex mixer (Fisher Vortex Genie 2, Fisher Scientific) to produce a suspension of PDMS prepolymer microspheres by emulsification. The emulsion was cured for 24 hours in an oven at 60°C.

In preparation for surface modification and subsequent compression, the cubes and microspheres were washed with de-ionized (DI) water and dried after curing. Surface modification of the PDMS cubes and microspheres was performed with radio frequency oxygen plasma (4 minutes, 0.5 Torr, maximum power, Plasma Prep II, SPI supplies) to generate a thin, silica-like film on the surface. Individual oxidized PDMS cubes were compressed using a manual micrometer-screw-driven compression apparatus (Micro Vice Holder; S. T. Japan USA, LLC. FL, USA). Compression of the microspheres was performed using a homemade system described in the next subsection. The compression induced periodic cracks in the surface layer, exposing the hydrophobic substrate, in both the cubes and spheres.

3.2.2 Compression of the cubes and spheres and crack-pattern observations

Oxidized PDMS cubes were uniaxially compressed to between 10 and 50% of their original side length (Figure 3.1a). An optical image of the crack patterns observed directly on a face of an oxidized cube, immediately after having been released from approximately 35-40% compression, is shown in Figure 3.1b. The applied compression

[1] An ethylene oxide/propylene oxide block copolymer surfactant

generated an ordered series of parallel cracks aligned with the direction of compression in the center of the cube face. The crack pattern deviated from being strictly straight and parallel near the edges of the cube face. On the side of the contacts there was a period of transition in the spacing of the cracks, from very sparse at the contacts to the higher density of the ordered cracks in the center of the cube face. At the free edges, the cracks disappear in the middle region between the contacts but change direction, from parallel to perpendicular to the applied compression, near to the contacts. Formation of the ordered crack pattern in the center of the cube face was controllable, adjustable, and reproducible in terms of the average crack spacing. Consistent with prior analyses and observations of thin-film cracking (*9-12*), the average spacing systematically decreased with increasing amount of compression.

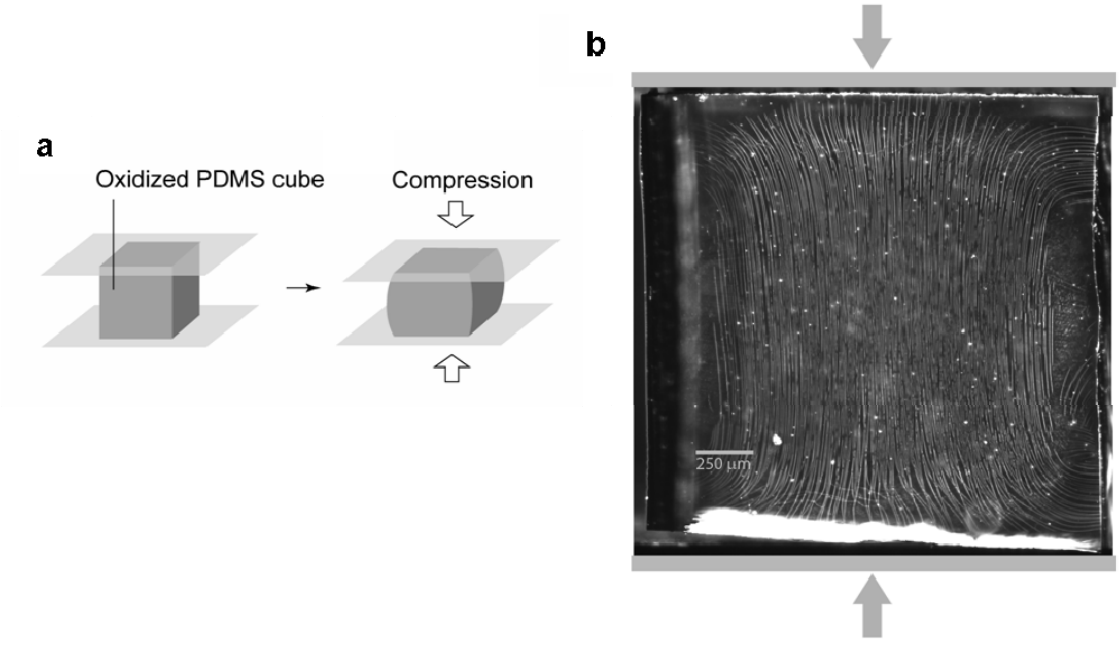

Figure 3.1 – Cube compression scheme and resulting crack patterns
a) Compression of an oxidized cube of PDMS (each edge: 2 mm, 1:10 curing agent-to-base ratio in weight). b) Compression with significant friction at the contacts (top and bottom) yields a non-uniform tensile stress oriented perpendicular to the direction of compression; consequently, cracks were produced in the brittle oxidized layer (Imaged with a 2X objective on the Nikon TE 300).

Despite the small size which precludes external stretching, compression of microspheres with diameters down to approximately 200 μm is still experimentally straightforward using manual procedures (Figure 3.2a). Fixed into a PDMS slab on the movable upper stage was an adhesive-covered specimen mount for use in the scanning electron microscope (SEM). The microspheres were placed on a bare specimen mount, oxidized, and then the mount was fixed beneath the upper stage. The microspheres were compressed between the two specimen mounts by lowering the upper stage. The amount of compression of the microspheres was controlled by using different numbers of glass coverslips (each 170 μm thick) as spacers between the specimen mounts (Figure 3.2a). The final percent of compression of each microsphere was calculated as

$$Compression \quad (\%) = \frac{d - t}{d} \times 100 \tag{1}$$

where d and t are the diameter of microspheres and the thickness of spacers, respectively.

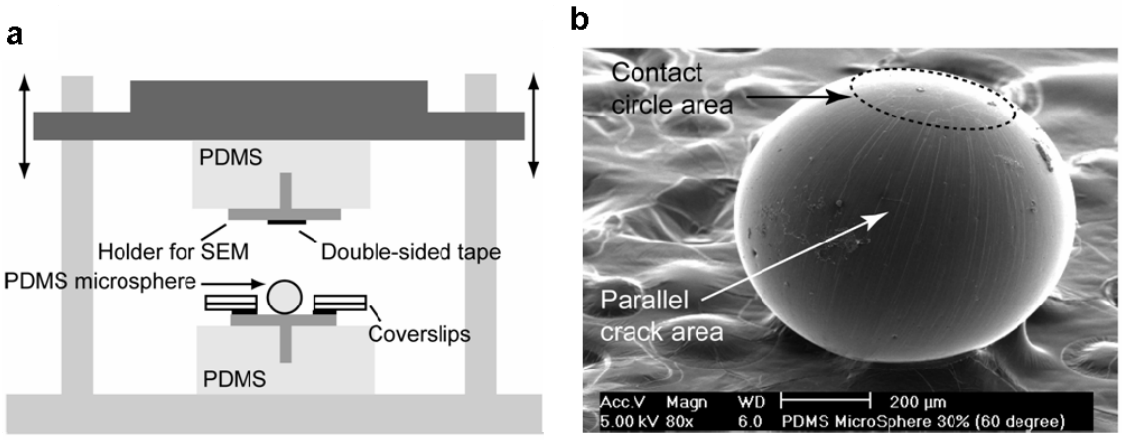

Figure 3.2 – Sphere compression scheme and resulting crack patterns
a. The device for controlled compression of the microspheres. B. SEM image of a microsphere that has been compressed by 30% of its radius. The contact circle area (2D random orientation of cracks) and the area between the two contact circles (parallel cracks running from pole to pole) are marked with arrows on the image.

With the microspheres fixed to the adhesive-covered specimen mount during compression, their subsequent transportation and handling were facilitated. In addition, their orientation with respect to the compression direction was known when obtaining images.

Oxidized PDMS microspheres were compressed to 33 ± 1%, 58 ± 1%, and 79 ± 1%, and the resulting crack patterns were studied in the SEM (Philips/FEI XL30FEG).[2] Several features are of note. (i) The imprint of the contact circle formed during compression is visible at the top pole of the microsphere (Figure 3.2b & Figure 3.4b). The radius of this contact circle provides confirmation of the degree of compression imposed. (ii) The cracks inside and along this contact circle are randomly oriented, most likely due to the contact with the specimen mount. (iii) Like compression of the oxidized PDMS cubes, compression of the oxidized PDMS microspheres also yielded parallel cracks (Figure 3.2b & Figure 3.4b).

Table 3.1 summarizes the values of the radius of the microsphere, the radius of the contact circle, and the crack spacing at the equator for three different percentages of compression, as defined by Eqn. (1). As expected, the radius of the contact circle increased and the crack spacing decreased with increased compression. In addition, the crack spacing on one microsphere, when measured anywhere outside of the contact circles, was reasonably consistent. This observation indicates that the amount of tensile strain in the oxidized layer does not significantly vary with distance from the equator. The tensile strain at the equator was determined using a series of finite-element simulations, of individual spheres under compression. The average crack spacing

[2] Prior to imaging, the relaxed PDMS microspheres were coated with carbon (SPI Supplies, Module Carbon Coater). Carbon coating was performed for 2 minutes.

Compression	79%	58%	33%
Microsphere radius, μm ± 2 μm	400	412	395
Contact circle radius, μm ± 15 μm	435	330	140
Crack spacing, μm	1.9 ± 0.3	3.8 ± 0.7	7.3 ± 0.6
Approximate equatorial circumferential tensile strain	60%	25%	7%
Crack spacing of Zhu, *et al*. 2005, μm	2.7 ± 0.6	6.4 ± 0.8	12.3 ± 5
Crack spacing of Mills, *et al*. 2007, μm (Ch. 2)	--	1.9 ± 0.6	7.5 ± 3

Table 3.1
Relationship between the amount of compression, contact circle radius, and crack spacing. Microspheres were chosen to have a radius equal to approximately 400 μm.

systematically decreased with increasing amount of calculated tensile strain. The crack spacing on the spheres is compared (Table 3.1) to the crack spacing obtained on flat surfaces of PDMS (rectangular slabs) that had been oxidized and strained in two different studies – the last row being values from Chapter 2. The discrepancy between the crack spacing for nominally the same PDMS preparation and oxidation conditions in the different studies is attributed, in part, to an inability to control the precise oxidation conditions between different runs (*62*).

3.3 Finite-Element Analysis and Discussion

Finite-element calculations were performed (using the commercial package ABAQUS) to understand the origin of the tensile stress in the oxidized layers required to produce crack patterns. The bulk PDMS was modeled using 3-D hybrid brick elements for the cubes, and axisymmetric hybrid elements for the spheres. The oxidized layer was modeled using 3-D linear-elastic shell elements for the cubes, and axisymmetric shell elements for the sphere. The properties of the bulk PDMS and the

surface layer were taken to be those obtained in earlier studies, with the thickness of the oxidized layer being assumed to be 200 nm (*62*). Compression was applied to the cube in the model by nodal displacements on the top surface of the cube while keeping the nodes on the bottom surface constrained in the same direction. Two extreme cases were modeled: one in which the nodes on the top and bottom surface were free to translate perpendicular to the direction of compression (the frictionless case) and one in which the nodes were constrained perpendicular to the compression (the no-slip case). Compression was applied to the spheres through a 2-D model of the aluminum compressing plates, with an elastic modulus of 70 GPa. The contact between the plate and the sphere was modeled as frictionless. Displacement control was used to compress the sphere to compression ratios of 20, 40, 60, and 80%. After compression, the sphere was allowed to relax in the numerical model. The radius of the contact circle was measured from the relaxed mesh (using points *P* and *Q* in Figure 3.3a). This final radius of contact was found to be equal to 460 μm for a sphere that had been compressed by 80%. This is in good agreement with the experimentally measured contact radius of 420 – 450 μm.

The finite-element calculations showed that the origin of the tensile stresses responsible for the crack patterns is different for the two geometries. In the case of the cube, *frictionless* contact produced tensile stresses *only if* the Poisson expansion of the bulk PDMS material was greater than that of the oxidized layer. The magnitude of the induced tensile stress depended on the modulus of the oxidized layer and the amount of applied compression, and was uniform across the surface (Figure 3.3). If there was significant friction at the contact between the compression device and the PDMS cube,

the resultant constraint caused the free surfaces of the PDMS cube to bow out. This caused a tensile stress to be induced perpendicular to the direction of compression – regardless of whether there was a difference in Poisson ratio between the film and the PDMS (Figure 3.3). The tensile stress induced by this mechanism depends on the magnitude of the friction at the contacts, and it varies over the free surface of the cube – higher stresses are induced in the center of the cube face as opposed to near the edges (Figure 3.3).

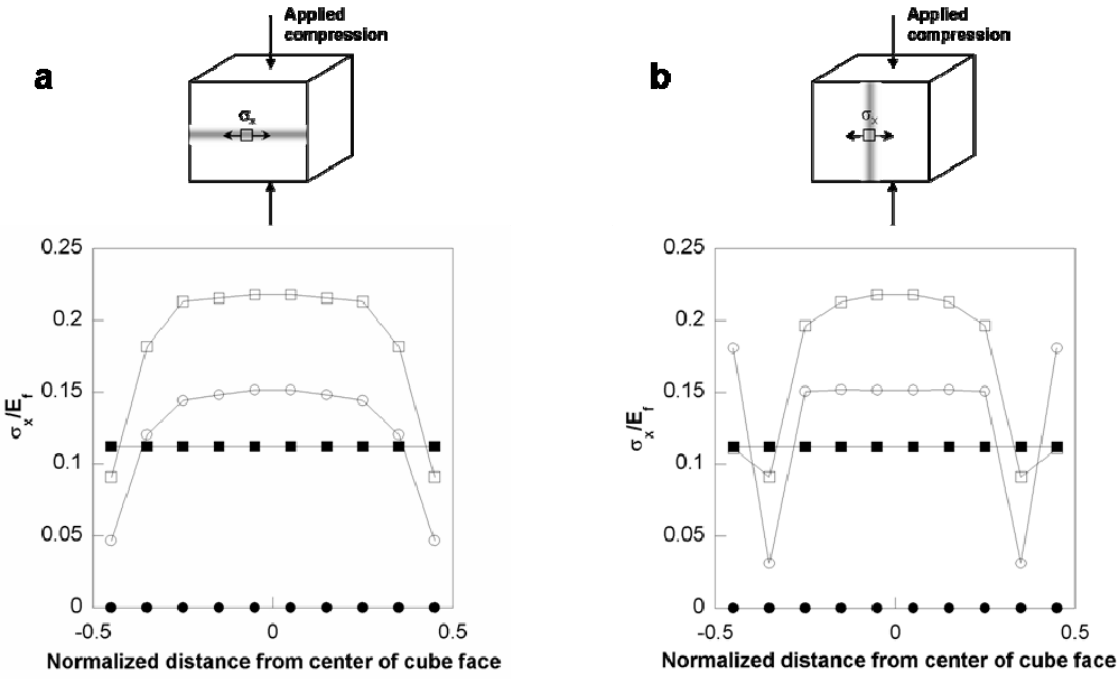

Figure 3.3 – Stress distribution on cube faces
Normalized stress in the surface-modified layer in the direction perpendicular to the applied compression along middle of the face from (a) side to side and (b) from top to bottom. The applied compression was 40% for all plots. Filled markers represent the results for the case of frictionless contacts (●:$\nu_s = \nu_f$; ■: $\nu_s \neq \nu_f$) Unfilled markers represent the results for the case of no slip at the contacts (○: $\nu_s = \nu_f$; □: $\nu_s \neq \nu_f$)

Oxygen plasma treatment of PDMS creates compositional changes in the oxidized layer consistent with a silica-like structure (*2, 3, 6, 31*) which may also

produce a decrease in the Poisson's ratio at the surface layer. This would account for the development of tensile stress in the surface layer due to the larger Poisson expansion in the bulk PDMS. However, experimental observations of the free surfaces of the cube bowing out under the applied compression indicate that friction at the contacts plays the more significant role in inducing the tensile stress. Additionally, the crack patterns on the surface of a cube (Figure 3.1c) are consistent with a non-uniform distribution of tensile stresses on the cube face (Figure 3.3), as the cracks were concentrated in the center 2/3 to 1/2 of the free cube face.

The finite-element calculations for the spheres allowed the circumferential stress normalized by the modulus of the surface layer, $\sigma_{\theta\theta}/E_1$, to be plotted as a function of the meridional coordinate ϕ (Figure 3.4c). It was noted that the circumferential stress is tensile in the absence of friction, even with no mismatch in the Poisson's ratio between the surface layer and the bulk PDMS. In this regard, the generation of tensile stresses is much more robust in the spheres than in the cubes. This tensile stress is consistent with the experimental observations of cracks growing perpendicular to the circumferential direction. The circumferential stress between the two compressing plates is relatively independent of the distance from the equator of the sphere (ϕ). This is consistent with the experimental observation that the crack spacing was relatively independent of ϕ.

It is of interest to note that the mechanics primarily responsible for inducing tensile stresses in the oxidized layer on the sphere are not the same as that for the cube. In the course of this study we recognized three mechanisms by which tensile stress may be induced in the surface layer of a 3-D shape subjected to an applied compression: (i) there is a Poisson's ratio mismatch between the surface layer and the bulk material, (ii) a

significant amount of friction is present at the contacts, and (iii) the shape has a non-uniform cross-sectional area along the axis of compression. It is this final mechanism alone that is mainly responsible for the tensile stresses necessary to induce the crack patterns on the sphere. To summarize, in right prismatic shapes, such as the cube, uniform axial compression alone does not induce a tensile stress perpendicular to the axis of compression despite the expansion of the material, due to Poisson's ratio, which induces a tensile strain. For this class of shapes it is necessary to have either a Poisson

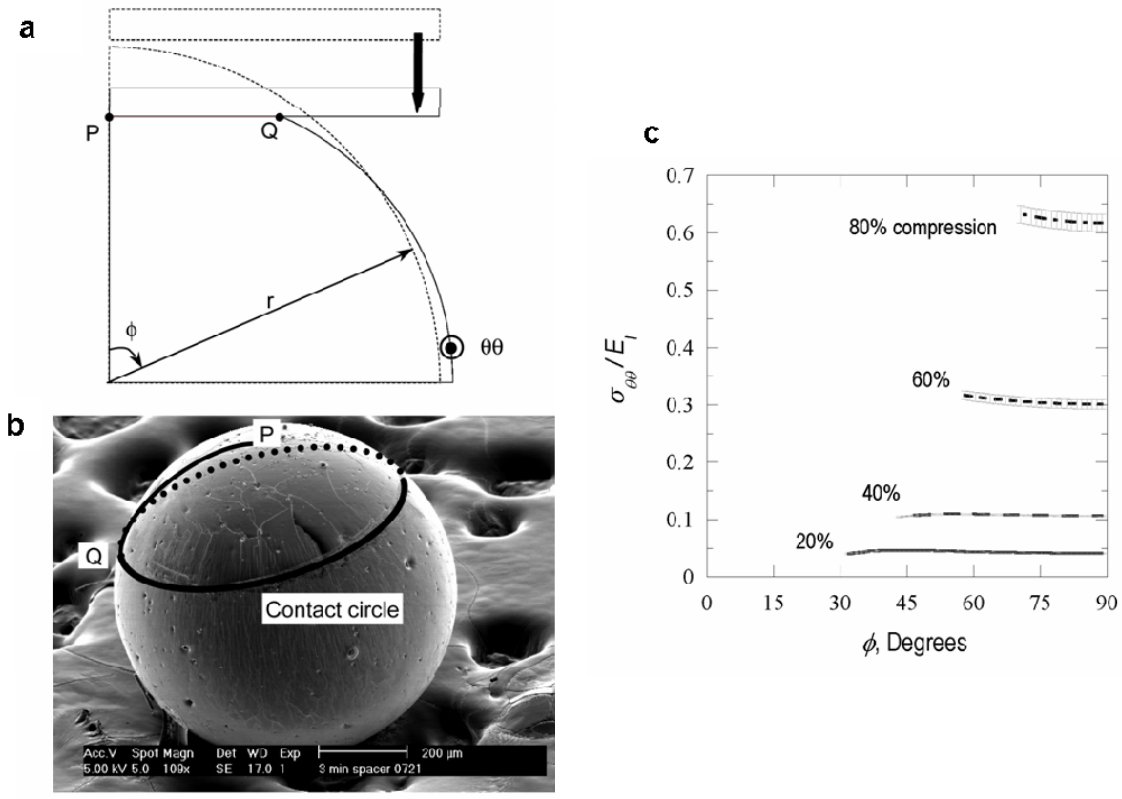

Figure 3.4 – Circumferential stress distribution on the sphere surface
a) A quarter axisymmetric model of the sphere and the upper compressing plate in the relaxed and compressed states. The distance between points P and Q are a measure the contact radius. The direction $\theta\theta$ is oriented pointing out of the page at the edge of the 2D representation of the microsphere. b) The experimentally observed contact circle whose radius was measured as the distance between P and Q as noted schematically on the image. c) The normalized circumferential stress with respect to meridional position, ϕ, at 20, 40, 60, and 80% compression (ϕ = 90° is coincident with the equator of the sphere). At all stages of compression the circumferential stress is tensile. The plots are terminated at the boundary of the contact circle.

ratio mismatch between the surface layer and the bulk material or friction at the contacts to induce the tensile stresses. Alternatively, in non-prismatic shapes, such as the sphere, when the cross-sectional area changes along the axis of compression, tensile stresses can be induced in the surface – even in the absence of any mismatch in material properties between the surface and substrate or friction at the contacts – simply due to their geometry. Although the details of the stress distributions vary depending on the shape, this provides a general guideline for predicting which shapes will yield cracking under various compression conditions.

3.4 Concluding remarks

In summary, the development of ordered crack patterns on the surface of PDMS cubes and microspheres by compression of the elastomeric polymer with a brittle oxidized surface layer has been presented. The fabrication technique that was proposed has three features that make it attractive: (i) it is easy and fast to implement and does not require expensive equipment; (ii) it can create ordered patterns on small objects where lithography, μCP, or stretch-induced patterning are difficult; (iii) the patterning method is scalable and increasing the number of microspheres or other objects that can be patterned simultaneously should be straightforward. Such capabilities may be particularly beneficial for applications such as self-assembly of patchy microspheres, where many patterned objects are needed (*13*). Although it is difficult to generate uniform patterns over the entire object, this technique is unique in its capabilities and has potential to be used to engineer functional small objects for materials science.

Chapter 4

Adjustable nanofluidic channels by tunnel cracking of a constrained brittle layer

4.1 Introduction

The success and proliferation of microfluidics has spawned significant interest in nanofluidics as techniques for nanofabrication are advanced and becoming more widespread. Nanofluidics research encompasses a very broad range of topics from chemistry to biology to physics; the promise of answers to fundamental questions in each is the goal. Some of the research being pursued includes the separation or sorting of molecules based on size (*63*), chemical affinity (*64*), or high-fidelity fluorescence detection (*65*). Furthermore, there is considerable interest in the controlled confinement and manipulation of single molecules. For example, several studies have been performed on the manipulation and elongation of DNA molecules in nanochannels (*17-21*) in order to analyze their biophysical static and dynamic properties. This topic provided the major motivation for the work presented here.

Current methods to fabricate nanochannels for molecular confinement consist of multiple steps often involving costly equipment (*16*). Furthermore, most of these methods produce static nanochannels with cross-sectional dimensions that cannot be changed during an experiment. Standard microfabrication techniques such as electron-

beam lithography, nano-imprint lithography, reactive ion etching (*66*), focused ion-beam milling, or the patterning of sacrificial layers are used to create the channel features in rigid substrates, generally silicon, SiO_2, or silicon nitride. After a pattern has been created, a bonding step is often required. The use of high temperature and pressure techniques, like anodic bonding, is not uncommon (*67*). There have also been some creative alternative means by which nanochannels have been fabricated. Among these is a method for creating open channels by which a diluted poly(dimethylsiloxane) (PDMS) mixture is directionally swiped onto a glass slide using lint-free towelettes for very small (3 nm x 160 nm) nanochannels (*68*). Another method used techniques borrowed from the communications industry. In a fashion analogous to that of drawing optical fibers, a polycarbonate millimeter-sized rectangular cross-section containing initial 30-μm sized microchannels was thermally drawn-down to end up with approximately 700 nm-diameter nanochannels (*69*).

The above techniques all have the limitation that the dimensions of the nanochannels cannot be changed once created. Recently, we have reported a method of using the cracking of a stiff oxidized layer on a compliant elastomeric substrate to produce nanochannels that may be subsequently deformed, using an externally applied weight, to produce an effective change in their cross-sectional dimensions (*7*). The use of an elastomeric material permits the employment of soft-lithography techniques for creating fluidic devices (*70*). Additionally, oxidizing the PDMS surface overcame the inherent problem of spontaneous adhesion due to surface forces that is a common issue with the creation of nanoscale features in this material (*7*). Furthermore, fabricating nanochannels in a compliant material presents a straightforward method for

dynamically changing the size of the channels – via mechanical deformation. This has been shown to be a valuable tool for triggering confinement-induced elongation of DNA molecules (*7*). Here, we further simplify the production and manipulation of the cracking-based nanochannels with an alternate fabrication method. It is anticipated that the method for fabricating nanochannels presented here will be advantageous for performing single-molecule studies in that the channel width can be easily controlled simply by applying a remote tension to the entire device.

In this Chapter, a cracking-based method for fabrication and manipulation of nanochannels is presented. This method is an extension of the method presented in Chapter 2 where, instead of cracking the free surface-modified layer of plasma-oxidized PDMS, the layer is sandwiched between two PDMS substrates before straining. We take advantage of the propensity of the stiff, brittle layer sandwiched between compliant, tougher substrates to produce an array of parallel tunnel cracks in response to an applied uniaxial tensile stress (*71*). Tunnel cracking has been previously studied in conjunction with matrix cracking of a brittle matrix composite (*72, 73*). When the tunnel cracks connect pre-fabricated microchannels, they can function as nanochannels. The relative ease with which the dimensions of the nanochannels may be changed – simply by applying or removing uniaxial displacements – makes this system ideal for dynamic size separation of heterogeneous populations of molecules or confinement of single molecules. In Section 4.2 a detailed description of the fabrication technique is presented. Some details on the behavior of the system and the characterization of the tunnel cracks – the origin of the nanochannels – are discussed in Section 4.3. Finally,

the results of experiments demonstrating the functionality of these nanochannels are presented in Section 4.4.

4.2 Materials and Methods

Fabrication of the nanochannels begins with casting PDMS prepolymer (10:1 polymer to curing agent) against a photolithographically-prepared SU-8[1] mold containing the positive of a pattern of two microchannels (width = 100 μm, height = 50 μm). The microchannels lie parallel to one another, 1 mm apart, over a length of 6.75 mm and angle away from one another at 30° on either end over a distance of 3.125 mm. The PDMS was then cured at 60°C for 12 – 15 hours. After curing, the PDMS was removed from the mold and a slab of PDMS (8.5 mm wide by 40 mm long) was cut to contain the pair of microchannels (Figure 4.1a). Inlet and outlet reservoirs were created at either end of the two parallel recessed microchannels by using a 1.5 mm-diameter biopsy punch to put holes into the molded PDMS.

Featureless thin films made from the same PDMS prepolymer were used for the second, mating substrate for the confinement of the nanochannels. These were created by depositing the prepolymer onto silane-treated glass slides and then using a spin coater (Brewer Science, Cee 100) to evenly coat the slides. The silane treatment ensured that the PDMS films could be easily removed from the glass slides in a later step. The PDMS-coated glass slides were placed in the 60°C oven for 12 – 15 hours. The thickness of the resulting PDMS thin films was determined to be approximately

[1] Epoxy-based photoresist, MicroChem

160 μm by using optical microscopy to examine small slices made with a scalpel blade that were attached to a glass slide.

Both the microchannel-patterned slab and the spin-coated film were cleaned using Scotch® tape. The microchannel-patterned substrate was placed on a paper tape-covered glass slide for rigid support, and both substrates were placed in a vacuum (40-60 mTorr) for 10-20 minutes prior to exposure to plasma oxygen for 60 minutes [Harrick Plasma, 30 W]. Immediately after the plasma treatment, the exposed surfaces of the substrates were mated, placing a small amount of pressure to the glass slides that sandwiched the substrates, to ensure conformal contact. Generally, this procedure was sufficient to create a permanent bond between the two substrates.

This technique of forming an irreversible bond is very useful and pervasive in the production of micro-fluidic and similar micro devices. The widely-accepted explanation for this phenomenon is that plasma oxidation changes the chemistry of the PDMS surface creating silanol groups (SiOH) at the expense of the methyl groups (Si-CH_3) (*74*). Upon bringing the two slabs of oxidized PDMS together, a condensation reaction occurs between the surface hydroxyl groups forming an Si-O-Si bond between the surfaces. Many researchers have validated this result; and, in some cases, parametric studies have been performed in order to determine the optimal oxidation conditions for consistent bonding (*75*) or the strongest bond (*76*). Analogous surface chemistry reactions take place during bonding of plasma oxidized PDMS to Si, SiO_2, silicon nitride, polyethylene, and glassy carbon (*74*) enabling the irreversible bonding of PDMS to these materials as well. In addition to creating the surface chemistry necessary for bonding, exposing PDMS to plasma oxygen creates a thin, stiff, surface-

modified layer (*62*). Over-exposure to plasma oxygen deteriorates the conditions necessary for bonding the oxidized PDMS owing to the creation of a thicker surface-modified layer that will not deform readily enough for the intimate contact necessary for bonding. The conditions for plasma treatment used in this study created a surface-modified layer that was easily bonded with the additional result of producing tunnel cracks upon stretching the device.

After bonding, the portions of the film not covered by the microchannel-patterned substrate were cut away using a scalpel blade and pulled off of the glass slide. Carefully, so as not to produce any handling strains in the bonded system which would introduce tunnel cracks in unfavorable orientations, the glass slide and the PDMS film – bonded to the nanochannels device – were separated. To do so, the exposed PDMS/glass edges were briefly soaked with ethanol while sliding the tip of a scalpel blade in between the glass and the PDMS film to release the bonded system without bending or twisting it. A representative drawing of the resulting bonded system is shown in Figure 4.1b.

The bonded device was loaded into a stretcher (Micro-Vice Holder) and a uniaxial tensile strain was applied that introduced tunnel cracks spanning the distance between the pre-patterned microchannels. The stretcher was fitted with a custom-built *X*-*Y* stage for an epi-fluorescence microscope (Olympus TE-300) which allowed for simultaneous observation of the tunnel cracks while straining. A 60X oil-immersion objective (Nikon Plan Apochromat, NA=1.40) or a 20X objective (Nikon Plan Fluorite, NA=0.45), depending on the experiment, was used and images were captured using a CCD camera (Hamamatsu ORCA-ER).

4.3 Observations and characterization of the nano-tunnels

Observations of the behavior of the tunnel cracks were made following the fabrication of the nanochannels device. The device was mounted into a stretcher and placed on an optical microscope platform so that the bonded area between the microchannels could be observed as a tensile strain was applied to the device. Tunnel

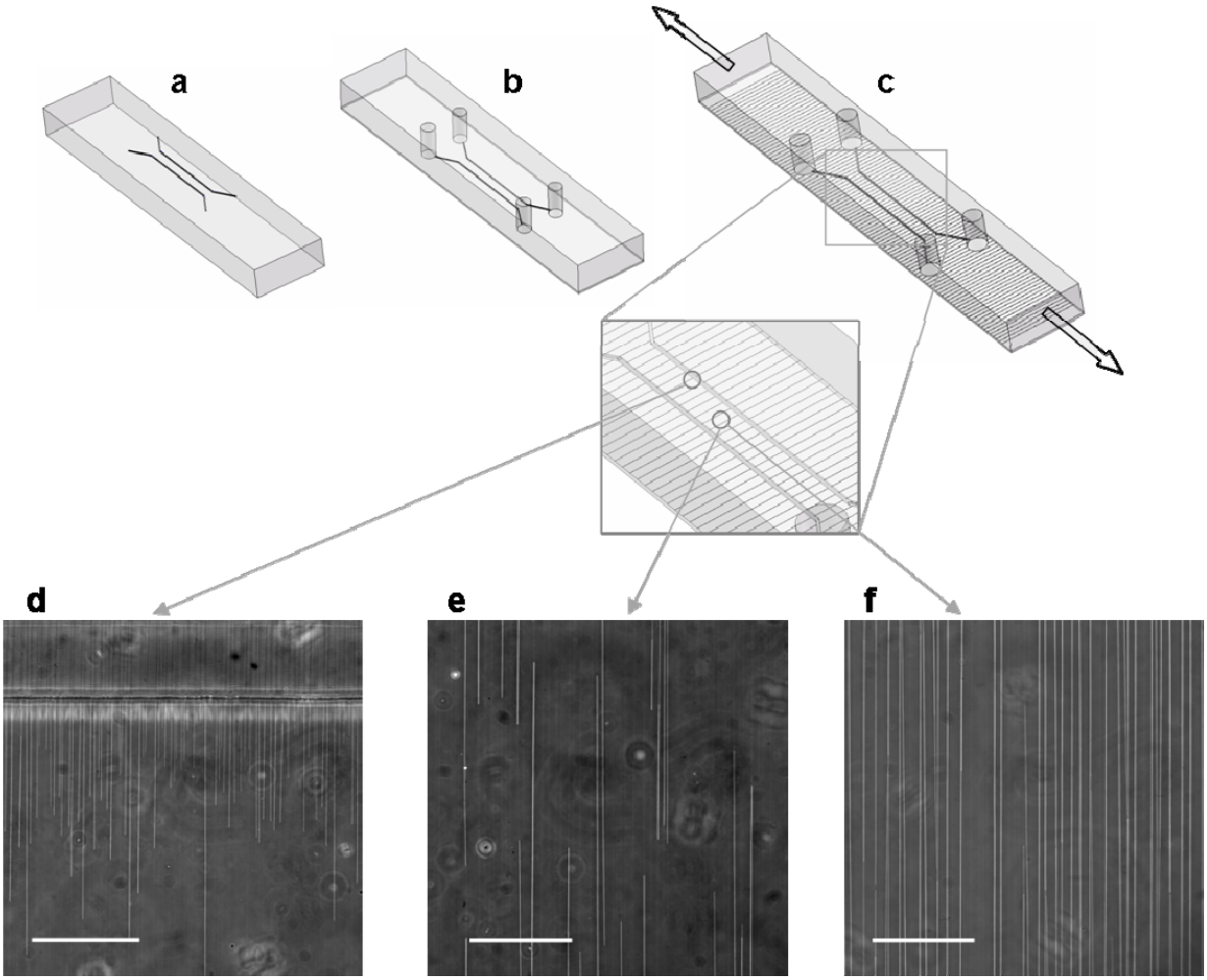

Figure 4.1 – Nanochannels device fabrication schematic and tunnel crack images
a. The molded PDMS slab (40 mm × 8.5 mm × 3.5 mm) containing depressed microchannel features (100 μm width × 50 μm height). b. The bonded system with 1.5 mm-diameter reservoirs at the ends of each microchannel. c. When the bonded system is stretched, a series of parallel tunnel cracks form which span the distance between the two microchannels, d-f. Evolution of the tunnel cracks with increasing applied strain. Scale bars are 100 μm. d. The boundary with the microchannel (top) is where the majority of the cracks are nucleated at a relatively small amount of strain (3%). e. With increasing applied strain, the cracks propagate from either microchannel towards the middle of the space between them (4-5%). f. The cracks completely traverse the space between the microchannels (~5%).

cracks were initiated within the surface-modified layer at the edges of the microchannels upon the application of a tensile strain in the range of 3% (Figure 4.1d). With increasing strain (4-5%), the tunnel cracks continued to propagate from either microchannel towards the area between them (Figure 4.1e), eventually connecting the two microchannels (Figure 4.1f) at approximately 5% with an average spacing of about 7.6 μm. Increasing the strain caused both the formation of new cracks, with an average spacing of about 3.3 μm being reached at 25% strain, and the enlarging of existing cracks. The cracks were estimated to be between 400 and 1000 nm wide when the device was stretched to 5% and between 700 to 1300 nm wide when stretched to 25% (Figure 4.2). Decreasing the strain caused the crack sizes to decrease and upon removal of the strain the cracks completely healed. Repeating the cycle caused the re-opening of the original cracks in a manner similar to that of the original sequence.

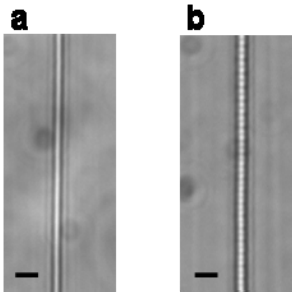

Figure 4.2 – High-magnification tunnel crack images
The nano-tunnels were estimated to be between (a) 400 and 1000 nm wide when the device was strained to 5% and between (b) 700 and 1300 nm wide when strained to 25%. Buckling of the nanochannels walls at the higher strains is caused by Poisson compression of the substrate along the direction of the tunnels, perpendicular to the direction of the applied strain. The scale bars are 2 μm.

The dimensions of the surface-modified layer were examined using a technique with the atomic force microscope (AFM) described in Chapter 2 (*62*). Two slabs of the PDMS were exposed to plasma oxygen for 60 minutes at a power of 30 W and then bonded. The bonded specimen was fractured to expose the bonded surface-modified

layers in the middle of a cross-section of unexposed PDMS. An AFM in tapping mode was then used to create a phase image of the resulting cross-section over the region of the bond. The phase image is shown in Figure 4.3c and d along with the 3-D and 2-D height images (Figure 4.3a and b). Although the bond is only slightly perceptible in the height images, there is a detectable feature in the phase image at the location of the bond. The phase image indicates that the boundary between the surface-modified layer and the PDMS is not smooth. The width of the feature in the phase image is between 450 and 1500 nm, from which it may be deduced that the surface-modified layer is between 225 and 750 nm thick.

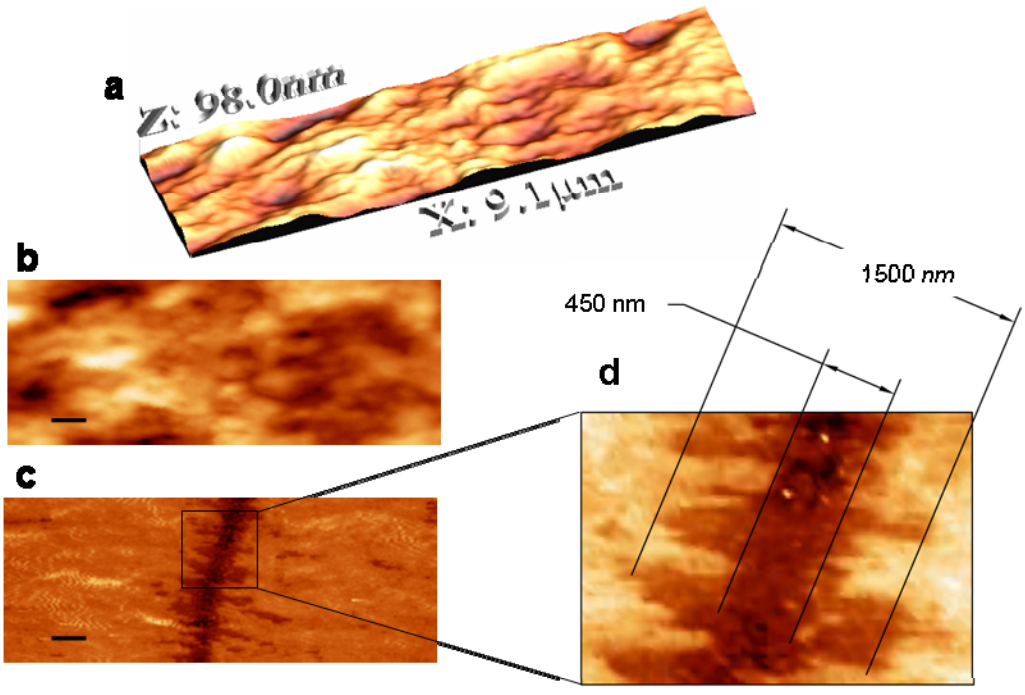

Figure 4.3 – AFM height and phase images of surface-modified layer cross-section
a. 3D height image of the cross-section containing the bonded surface-modified layers. b. The corresponding 2D height image. c. 2D phase image of the bonded cross-section clearly identifying the bond plane, the range of phase angle is 0 – 45°. Scale bars are 500 nm. d. Dimensions on a zoomed section of Figure 4.3c showing the total thickness of the two surface-modified layers bonded together.

A further experiment was performed to compare the tunnel cracking observed in the bonded system with the channel cracks observed in earlier work where the PDMS was not bonded (*1, 62*). Two slabs of PDMS and one film of PDMS were oxidized for 60 minutes at an RF power of 30 W. One of the PDMS slabs was bonded to the film and then strained to 25% and the other slab was left unbonded and strained to 25%. The tunnel and channel cracking behavior of the two specimens was compared. Figure 4.4a and 4.4b show optical images of the tunnel and channel cracks, respectively.

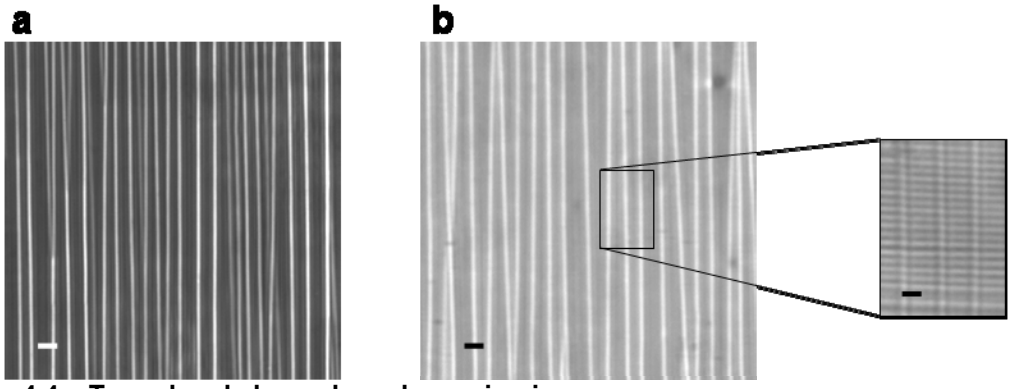

Figure 4.4 – Tunnel and channel crack spacing images
a. Nanochannels created by tunnel cracking in bonded surface-modified layers of PDMS.
b. Channel cracking in the surface-modified layer of PDMS. Inset: Buckling of the surface-modified layer is present perpendicular to the cracks. The surface buckling is suppressed when the surfaces are first bonded together and then strained. The applied strain is 25% in each case. Scale bars are 5 μm.

The crack spacing of both the tunnel and channel cracks was then measured optically. The distributions of crack spacing for each are plotted in Figure 4.5 and were observed to fit Poisson distribution $\left(p_{L_{ave}}(L_i) = \frac{e^{-L_{ave}} L_{ave}^{\ L_i}}{L_i!} \right)$, with an average spacing, L_{ave}, of 3.3 ± 1.2 μm for the tunnel cracks and 4.6 ± 1.4 μm for the channel cracks. This distribution depended on the level of applied strain, with the average spacing decreasing as the strain was increased. Mechanics analyses of cracks in surface (*10, 12*) and

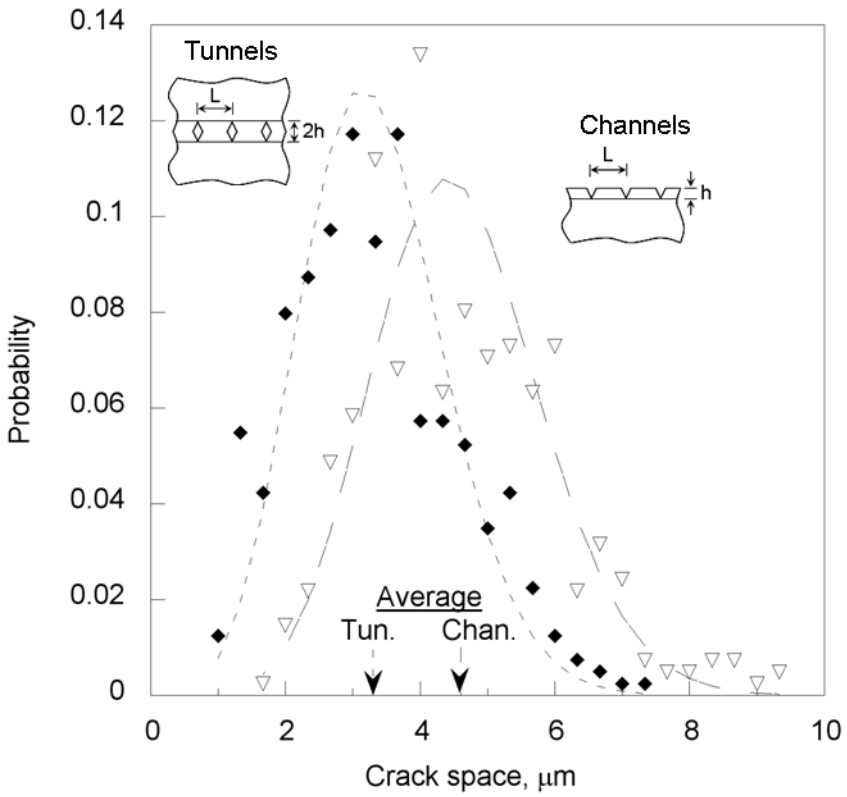

Figure 4.5 – Tunnel and channel crack spacing distributions
The distributions of crack spacing for the tunnel and channel crack configurations at 25% strain.

sandwich layers (*71*) indicate that the equilibrium spacing of cracks should increase with the thickness of the layer (and crack depth), and should be smaller in a sandwich layer of the same thickness. Physically, the increased crack density in the bonded sample occurs because of the additional constraint provided by the surrounding substrates. This point is illustrated very clearly by the data of Figure 4.5. Even though the bonded layer is expected to be twice as thick as the unbonded layer, the spacing of the tunnel cracks in the sandwich layer was significantly smaller than the spacing of the channel cracks in the unbonded surface layer.

4.4 Nano-fluidic applications and results

An additional preparation was required to achieve wetting of the nanochannels before using them for fluidic applications. The difficulty of wetting was probably caused by the fact that the tunnel cracks may extend from the hydrophilic layer, in which they are formed, into the unmodified and hydrophobic substrate. Therefore, the surfaces of the nanochannels may be composed of a central hydrophilic region flanked by hydrophobic regions.

Two different procedures were explored to enhance the wetting of the nanochannels. In one procedure, the nanochannels were further treated with plasma oxygen to render their surfaces hydrophilic. This was achieved by immediately loading a bonded device into a custom-built screw-driven slider and rail stretching system and applying a strain between 15 and 20% while exposing the system to plasma oxygen at 30 W for an additional 30 minutes. (However, this amount of strain did occasionally cause the device to fracture during the oxidization process.) In the second procedure, the solution that was to be used in the application of interest was introduced into both microchannels immediately after bonding and before the device was strained for the first time. Several cycles of straining and relaxing between zero strain and the maximum strain at which the device was to be used (approximately 25-30%) were applied. This created a pumping action which coaxed the solution into the nanochannels.

4.4.1 Electrokinetically driven flows of fluorescein molecules

To show that the nano-tunnels completely spanned the distance between the microchannels, a flow of a solution of fluorescein isothiocyanate (FITC)–dextran

(molecular weight = 500,000 Da) and deionized (DI) water was followed from one microchannel to the other. After a bonded system was fabricated, one microchannel was loaded with pure DI water and the other microchannel was loaded with the fluorescein solution. After several cycles of straining to wet the nanochannels, a tensile strain of approximately 10% was applied to hold open the nanochannels as the fluid started to fill the nanochannels. A voltage potential (32 V/cm) was applied across the fluidic circuit driving the fluorescein solution to the opposite microchannel and a sequence of images was taken (with representative images shown in Figure 4.6a). Intensity measurements, averaged over the center ¼ area of the outlet microchannel, were taken from these images. The resulting data (Figure 4.6b) indicated that it took 2.5 minutes for an equilibrium concentration of the fluorescein solution to be established in the outlet microchannel.

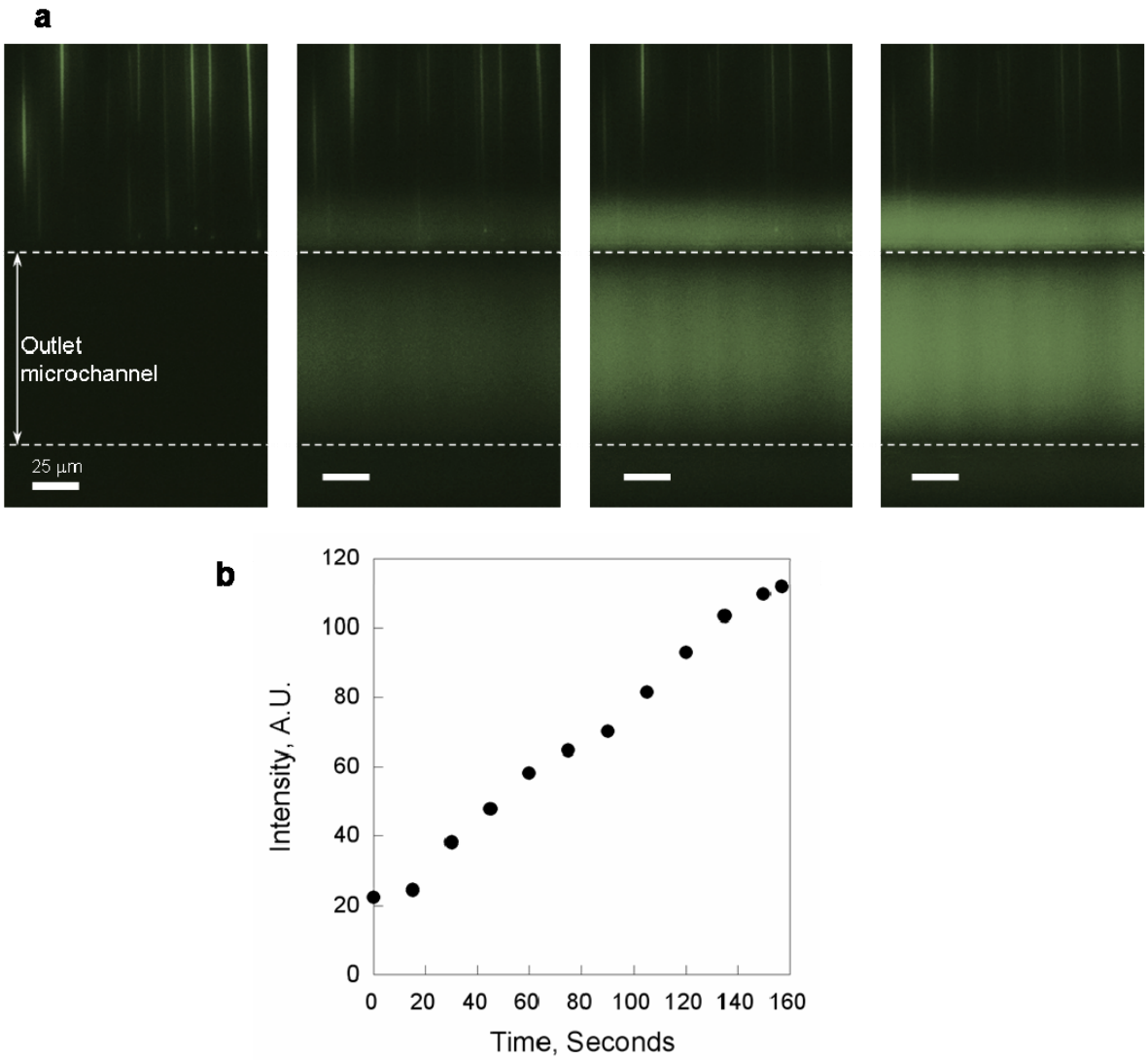

Figure 4.6 – Electrokinetic flow of fluorescein through the nanochannels
a. A series of images at elapsed times (0, 60, 120, and 160 seconds) from the introduction of the fluorescein solution into the outlet channel. b. Rate of fluorescence intensity increase as a solution of fluorescein and DI water was introduced into the outlet channel. Measurements were averaged over the center 1/4 of the channel along the complete length captured in the image field. The flow of fluorescein molecules was driven electrokinetically by 32 V/cm.

4.4.2 Electroosmotic manipulation of quantum dots

A solution was prepared containing DI water with a suspension of quantum dots (Qdot 605 Streptavidin Conjugate, Qdots). The quantum dots have a layered structure with the innermost layer being the semiconductor material cadmium selenide (CdSe) followed by a shell of another semiconductor material, zinc sulfide (ZnS). The zinc sulfide shell provides an enhancement to the optical properties of the quantum dots. A polymeric coating encases the semiconductor materials to which streptavidin molecules are couples. To image the quantum dots, they are exposed to fluorescent light with a peak excitation wavelength of 425 nm and they emit light with a peak emission wavelength of 605 nm which is detected with an optical microscope using a 60X objective. The solution of DI water and quantum dots was injected into both of the microchannels. Because the nanochannels had been treated with plasma oxygen after being created, the quantum dot solution filled the nanochannels when the device was stretched to 10%. There was no need for the repeated cycling described in the previous section. A flow of the quantum dots was driven electroosmotically by an applied electric field with magnitudes ranging from 10 to 40 V/cm. The quantum dots were observed to flow towards the negatively charged electrode and upon reversal of the electric field they changed direction. Finally, releasing the strain closed the nanochannels effectively trapping the quantum dots.

To determine the sensitivity of the flow of the quantum dots to the electric field, their position was tracked in a sequence of images captured for each of a series of applied voltage potentials. The applied strain was held constant at 10% and the flow of two quantum dots was followed for voltage potentials of 13, 23, 30, and 39 V/cm. As the quantum dots approached the edge of the field of view, the polarity of the electric

field was changed so that the quantum dot travel reversed direction. As expected, the velocity of the quantum dots increased with increasing magnitudes of electric field (Figure 4.7a). An observation during the experiment is of note. The quantum dots did not traverse the nanochannels at a steady-state flow rate. Rather, they followed a

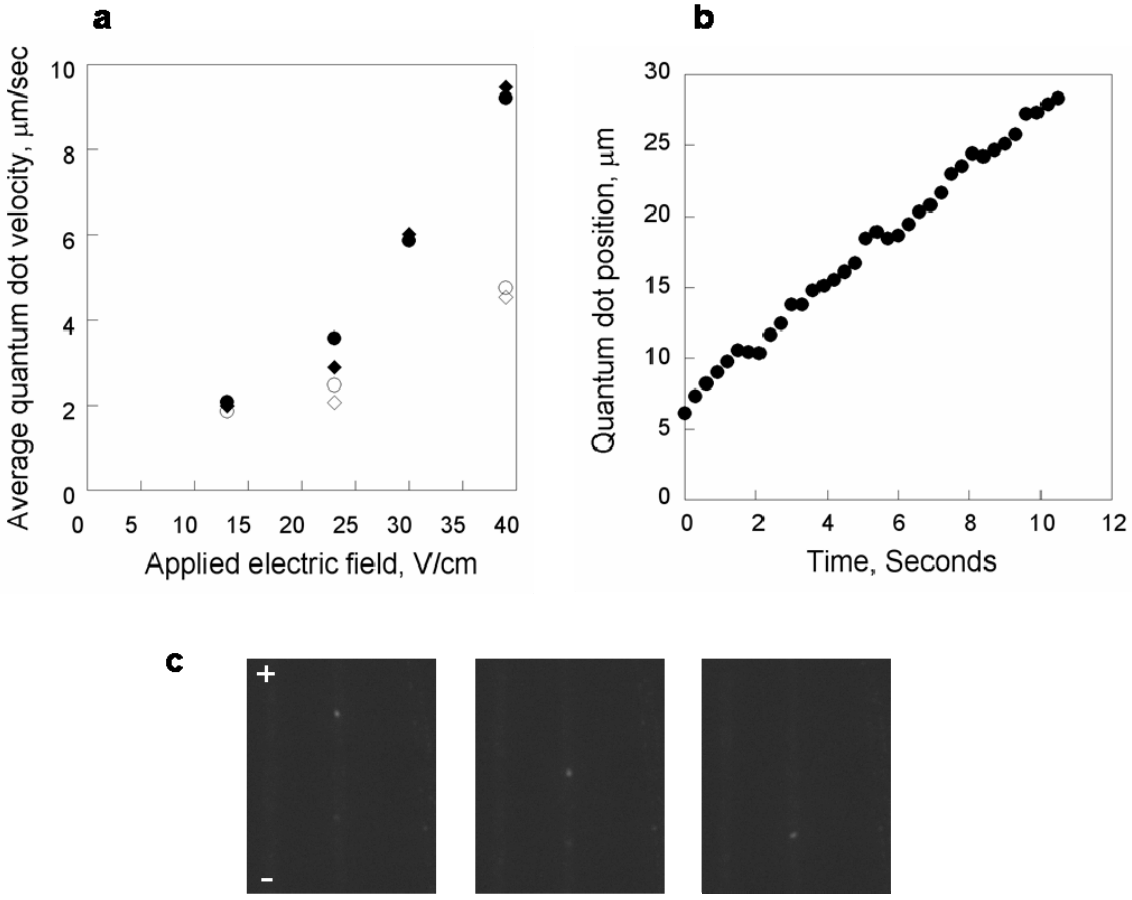

Figure 4.7 – Electroosmotic flow of quantum dots through the nanochannels
a. The average velocity of two different quantum dots (diamond and circle markers) subject to various different levels of an applied electric field. The polarity of the electric field applied across the nanochannels was changed periodically which resulted in a higher velocity (filled markers) as the quantum dots traveled in one direction than in the other (unfilled markers). b. The typical stop-and-start behavior of a quantum dot as it travels through a nanochannel. A voltage potential of 23 V/cm was applied across the nanochannels in this case but the behavior was common at all potentials. c. A sequence of images of a single quantum dot traveling in a nanochannel under an applied electric field of 13 V/cm. The applied strain was held constant at 10% for all measurements in this figure.

pattern of stopping and vibrating in place before starting again with a relatively constant rate before stopping again several microns later. This is most likely due to an adhesive interaction between the quantum dots and the walls of the nanochannels (*77*). A representative plot of quantum dot position with time showing this behavior is shown in Figure 4.7b.

4.4.3 Electrical resistance measurements across nanochannels

The extent to which the size of the nanochannels could be varied by strain was quantified by taking measurements of the electrical resistance across the nanochannels. After bonding the device, but before forming the tunnel cracks, a solution of 0.1 molar potassium chloride (0.1 M KCl) was injected in to both microchannels. Silver/silver chloride (Ag/AgCl) electrodes (Warner Instruments, Ag/AgCl pellet electrodes, E205) were inserted into each end of a single microchannel. A constant voltage potential (0.1 V DC) was applied across the electrodes and a resistance of 945-950 kΩ was measured using a picoammeter (Keithley Instruments, Inc., Model 6487). The dimensions of the microchannel given in Section 2 were used to compute the resistivity, ρ, of the 0.1 M KCl which was found to be 0.3 Ω·m.

The device was then mounted into a stretcher and the electrodes were inserted into the diagonally opposed inlet reservoirs of the two microchannels. A very high resistance (on the order of 1-10 GΩ) was measured before stretching, consistent with the insulating nature of the PDMS and a lack of any direct electrical connectivity between the microchannels. The device was then strained to 25% and completely unloaded several times to create tunnel cracks and ensure that they were filled with the KCl solution, as verified with an optical microscope.

After it was determined that the nanochannels had filled with the KCl solution, they were held open by subjecting the device to a tensile strain of 26% and the resistance, in this state, was determined to be 1.5 MΩ. The strain was then relaxed in small increments of 2.6% and the resistance was measured after the device had been held at the new strain for one minute. There was a monotonic increase in the resistance as the strain was decreased which is assumed to be associated with the closure of the tunnel cracks. Once reaching the fully relaxed state, the device was held for one hour. During this time, the resistance increased by an order of magnitude, from 100 MΩ to over 1 GΩ. It should be noted that the latter value is comparable to the resistance measured before any cracks formed and would seem to indicate that almost complete closure and exclusion of the KCl solution occurred during this period. The experiment was then repeated in reverse: resistance measurements were taken after the applied strain was increased in increments of 2.6% and held for one minute. Upon returning to 26% strain, the device was again held for one hour during which there was no significant change in the resistance. The maximum strain was then increased to 31% and a second cycle was started, unloading at the same rate as during the first cycle. After reaching the fully unloaded state, the device was held for only one minute before loading and unloading once more at the same rate with a one-minute hold in between. Figure 4.8 shows the results for the complete two and a half cycles.

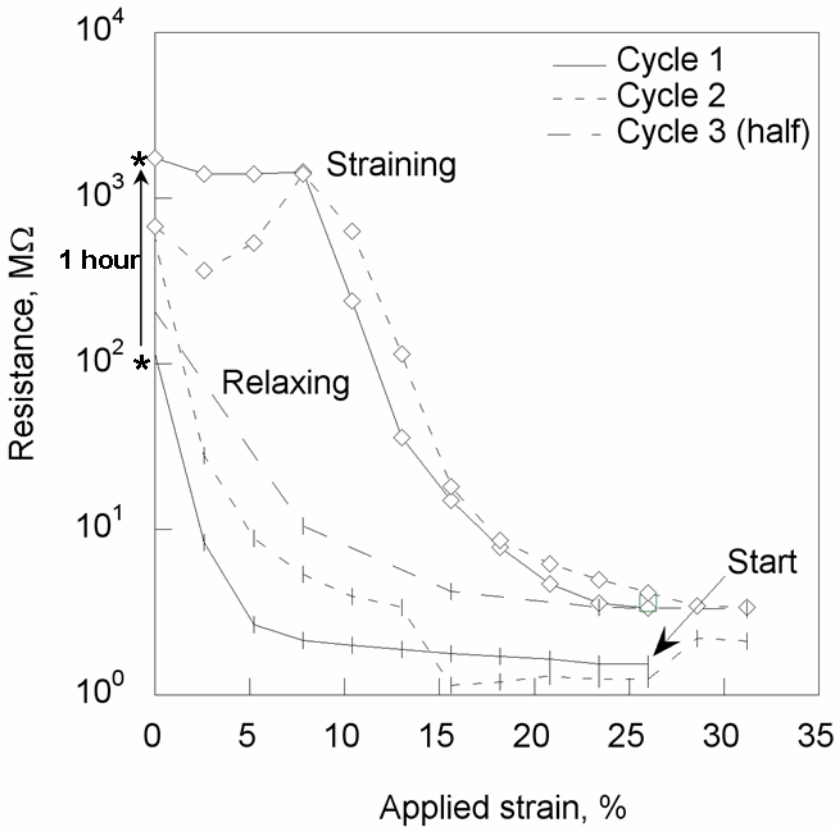

Figure 4.8 – Electrical resistance measurements across nanochannels filled with KCl
Electrical resistance measurements were taken on the device with the nanochannels filled with a 0.1 M KCl as the applied strain was being varied from a maximum of 31% to the fully relaxed state. For comparison, the resistance measured before tunnel cracks were introduced was on the order of 1-10 GΩ and the resistance measured across a microchannel filled with 0.1 M KCl was 945-950 kΩ.

The general features discussed in the previous paragraph of an increase in electrical resistance with a decrease in strain are clear from this plot. However, there are a few other features that are of note. First, the complete collapse of the nanochannels in the fully-relaxed state is time-dependent. Since earlier studies had shown that the deformation of PDMS had very little time-dependence, the time-dependence exhibited here is probably associated with the flow of fluid with the nanochannels. Second, a tensile strain of approximately 10% is required to open the collapsed cracks. This appears to be the level of strain required to provide a sufficient

level of energy-release rate to overcome the surface forces that are holding the tunnel cracks closed. In this regard, the behavior of the cracks during the second loading cycle (which did not have a prolonged hold at the fully relaxed state) is informative. When the applied strain is below 10%, the cracks are attempting to close due to the thermodynamic state of the system, but closure is resisted by the presence of the fluid. Eventually, the cracks collapse completely, but then the strain increased sufficiently to open them again. Finally, there is hysteresis in the resistance measurements between the loading and the unloading curves: the cracks are either more open or there are more cracks open for a given strain during unloading. Unlike the hysteresis that commonly exists between crack extension and closure in fracture studies, this particular example appears to be associated with kinetic rather than equilibrium considerations. The reason for this behavior may be related to the fact that the cracks can open without fluid flow (and the fluid can then flow into a relatively wide tunnel crack), whereas the crack cannot completely close without the fluid first flowing out.

Knowing the resistivity, ρ, of the KCl solution it was possible to use the resistance measurements to estimate the average cross-sectional area of the nanochannels. The sum of the area of the tunnels spanning the distance between the microchannels is given by $A_{5o5ql} = \frac{\rho \ell_{ave}}{R}$, where R is the measured resistance and $\mathtt{l}_{ave}$ is the average distance between the microchannels which is 1.7 mm from the geometry of the microchannels. At the maximum strain, the average crack spacing was found to be about 4.8 μm. Hence, the average area of each crack under conditions of maximum strain is about 5.2×10^{-13} m^2. If the tunnel cracks are assumed to be diamond-shaped, with a width of about 1 μm (consistent with the measurements of Figure 4.2), the height

would be 520 nm. This estimate is consistent with what might be expected from the thickness of the oxidized layer measured in from the AFM phase images of Figure 4.3c and d.

4.5 Concluding remarks

A simple method for quick and easy generation of hundreds of parallel, size-adjustable nanochannels has been developed and tested. This method fabricates nanochannels, which are adjustable from over a micron in width to completely closed, approximately 3 to 7 microns apart and spanning the distance between two parallel microchannels. Continuous flow from one microchannel to the other was verified by measuring the accumulation of fluorescein molecules as they entered an outlet microchannel having been electrokinetically driven from an inlet microchannel. Control of the rate of flow in the nanochannels was investigated by tracking the position of individual quantum dots as they were electroosmotically driven with varying levels of applied electric field. Finally, a relative measure of the size of the nanochannels with respect to applied tensile strain was provided by electrical resistance measurements across the device.

Chapter 5

Nano-scale adhesion mechanics

5.1 Introduction

Compliant elastomeric materials are commonly used to manufacture devices with increasingly small features for use in micro- and nano-fluidics or for use in soft-lithography techniques such as micro-contact printing. The stability of the nano-structures or surface features against deformations due to surface forces is a very relevant concern on this length scale considering that the substrates can have an elastic modulus as low as 1 MPa. One mechanism by which these small structures may be affected is the distortion, or rounding, of perhaps otherwise sharp features, or corners (*22, 23*). Another, and the subject of this Chapter, is the adhesion of two free surfaces to one another, whether desirable or not. Finite-element calculations are used with energy arguments to investigate the conditions of collapse for features of various shapes and aspect ratios.

Adhesion or compressive deformation can cause collapse of the structures or the features that one would rather have remain structurally intact. Experimental observations as well as numerical analyses have confirmed this phenomenon for both free-standing micro- to nano-structures as well as the collapse of the "roof" of

rectangular recessed stamp features. Zhou, Huang et al. (*78*) showed that the collapse, when no applied compression is present is most likely caused by the release of surface energy when there is adhesion between the PDMS and the substrate. This result was based on a comparison of the experimentally determined profile of the deformed roof and that of finite-element calculations systematically taking into account the deformation due to surface adhesion, electrostatic force and the weight of the PDMS. Huang, et al. (*24*) then presented a numerical analysis of roof collapse based on this observation. The rectangular stamp features were approximated as coplanar cracks with the total potential energy being determined from the analytical solution for the stress field. In that analysis it was shown that the collapse was well described by the non-dimensional parameter $8a\gamma/E'h^2$ - or the ratio of adhesion energy to elastic deformation energy. Several groups have also studied the independent effects of an applied compressive stress field on the collapse of the roof of the rectangular stamp features (*26, 79, 80*). Hui et al. (*22*) analytically solved for the conditions of roof collapse by applied compression also based on the solution of the governing plane strain partial differential equations for coplanar cracks.

Besides rectangular features there is interest in nano-scale features of different geometries dependent on what exactly they are to be used for. Recently, nano-channels have been produced with a triangular cross-section and, with the optimal combination of size and elastic properties near the surface, they have been experimentally shown to be stable against spontaneous collapse as well as have the capability to be reversibly modulated (*7*). The triangular shape in this case was shown to be advantageous in that closure could be continuously controlled by an applied compressive stress in contrast to

the sudden yet partial jump to collapse of the middle of a rectangular feature. An easy-to-use tool is desired for the design of nano-scale features for soft-lithography and nano-fluidics that will not collapse in the absence of applied compressive stress and sometimes in the presence of a small compressive stress and to understand the capabilities of reversibly modulating the cross-sectional area. In Section 5.2, the effects of geometry, elastic properties, and both applied and surface forces on the stability of the triangular nano-scale features are studied. Section 5.3 focuses on the development of a generalized model for applying non-uniform surface tractions due to adhesive interactions between two surfaces.

5.2 Triangular nano-channels

5.2.1 Description of the experimental and finite-element models and numerical calculations

Triangular nanochannels (Figure 5.1) were fabricated using a multi-step method starting from the introduction of a series of parallel channeling cracks in the nano-scale surface-modified layer that is created on PDMS upon exposure to plasma oxygen. The properties of the surface-modified layer were estimated and the cracking behavior was studied in previous work (*62*). Following cracking, an epoxy replica was made of the cracked surface; and subsequently, a positive replica with recessed triangular channels was cast, in PDMS, off of the epoxy mold. Finally, the PDMS replica was exposed to plasma oxygen for a short period of time (30 seconds – 1 minute) and bonded to a piece of PDMS with no surface features (*7*). The compressive stress for actuation of channel closure was applied to the system by placing the necessary amount of weight on top of the device (*7*).

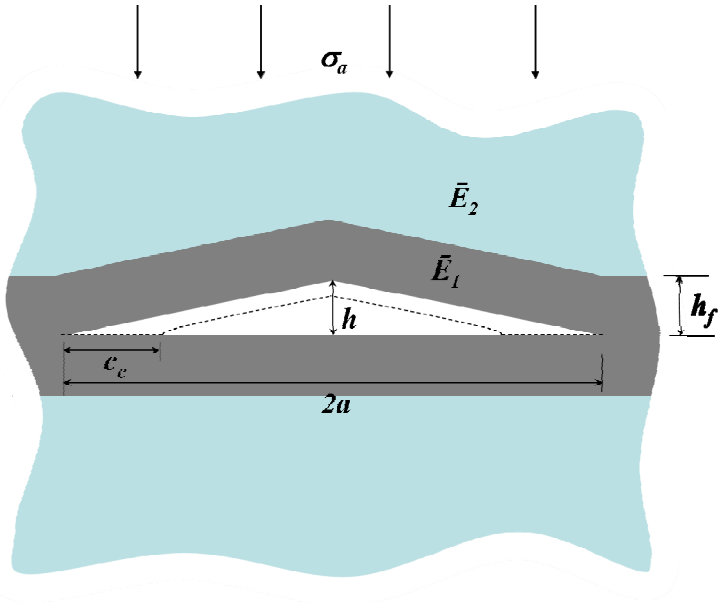

Figure 5.1 – Triangular nanochannel cross-section schematic
The schematic of the cross-section of a triangular nano-channel created by cracking of a nano-scale surface-modified layer on PDMS.

To study the energy of the experimental triangular nano-channel system as bonding proceeds, finite-element calculations were performed. The triangular nano-channel geometry was described by a half-base length, a, and initial height, h_0 (Figure 5.1). Due to the effect of surface forces and/or the applied compression, the closure of the triangle proceeded gradually from the corners and found an equilibrium position at the critical extent of closure, c_c. When oxidized, the PDMS had a surface-modified layer associated with it of thickness h_f, which is dependent on the amount of time that the PDMS was exposed to the plasma oxygen (*62*). The symmetry of the periodic triangular nano-channels was taken advantage of in the design of the finite-element mesh: a quarter-model of the geometry was used with appropriate symmetric boundary conditions (Figure 5.2). Both the PDMS and the surface-modified layer were meshed with 2D hybrid plane-strain elements. The hyperelastic material model was

used for the PDMS with tabulated uniaxial test data input directly for the specific behavior. The surface-modified layer was modeled as linear elastic.

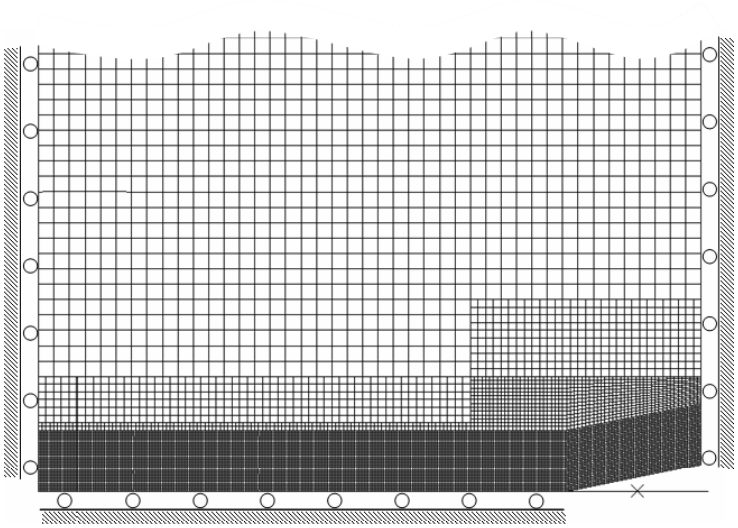

Figure 5.2 – Finite-element mesh for nanochannel adhesion studies
Finite-element mesh of the quarter-model nano-channel with schematic boundary conditions.

When two surfaces are close enough to be within the range of surface forces, whether they bond or not depends on the difference in total energy between the bonded and unbonded states. This energy is the difference between the elastic energy of deformation, associated with deformation of the bulk required for the surfaces to meet, and the surface energy released by mating the two surfaces.

$$U_{total} = U_{elastic} - U_{surface\ energy} \tag{1}$$

For the particular geometry considered in this Section, dimensional analysis shows that the total energy must be controlled by the following set of non-dimensional groups:

$$U_{tot}^{*} = \frac{U_{tot}}{\overline{E}_2 h^2} = f\left(\frac{c}{a}, \frac{h}{a}, \frac{\overline{E}_2 h_0^{\,2}}{\gamma a}, \frac{\overline{E}_1}{\overline{E}_2}, \frac{h_f}{h_0}, \frac{\sigma_a}{\overline{E}_2}, \nu_1, \nu_2\right), \tag{2}$$

where $\overline{E}_2$ is the plane-strain modulus of the bulk PDMS, $\overline{E}_1$ is the plane-strain modulus of the surface-modified layer, and σ_a is the applied compression. The non-

dimensional length scale, $\bar{E}_2 h_0^{\,2}/\gamma a$, will be shown to be a very important parameter in determining the behavior of bonding surfaces as it was also determined to be by Huang, *et al*. (*24*).

Finite-element analyses were carried out using the commercial package ABAQUS. To emulate the closure of the nano-channels by surface forces, the nodes of the triangular ceiling were pulled closed (vertically), one-by-one, starting at the corner of the nano-channel. At many intermediate extents of bonding (*c/a*), the deformation energy, $U_{elastic}$, was calculated as $\int_0^c \frac{1}{2} P(x)h(x)dx$, the integral over the length of closure (*c*) of the load necessary to close the nano-channel times the height of the nano-channel. At the same time, the surface energy released, $U_{surface\ energy}$, was calculated using $2c\gamma$. Once the two energy terms were determined it was possible to calculate the total energy of the system, U_{total}, using Equation 1. The total energy could then be plotted against the length of closure, *c/a*, and the critical closure distance (c_c/a) was defined as the minimum of this curve. The critical closure distance was determined as a function of the nondimensional length scale, $\bar{E}_2 h_0^{\,2}/\gamma a$; the modulus mismatch ratio, $\bar{E}_1/\bar{E}_2$; the aspect ratio of the triangular nano-channels (h_0/a); and the normalized compressive stress, $\sigma_a/\bar{E}_2$.

5.2.2 Discussion of numerical results

5.2.2.1 Dependence on non-dimensional length scale

The non-dimensional total energy, U_{tot}*, is plotted against the length of closure (*c/a*) in Figure 5.3 for a nano-channel created with unmodified PDMS ($\bar{E}_1 = \bar{E}_2$) and for three different values of the non-dimensional length scale. The critical closure

distance – the minimum in the total-energy curve – is dependent on the value of the non-dimensional length scale (Figure 5.3). For unmodified PDMS, the non-dimensional length scale is effectively the ratio of the modulus of the PDMS to its surface-energy. With a relatively low modulus as compared to the surface energy, as in the curve for $\bar{E}_2 h_0^{\,2} / \gamma a = 11$, the nano-channel completely bonds as indicated by the minimum at $c/a = 1$. Increasing the ratio of the modulus to the surface energy tends to prevent the complete closure of the nano-channel (e.g., Figure 5.3, $\bar{E}_2 h_0^{\,2} / \gamma a = 17$); and, if the non-dimensional length scale is large enough, there may be no energy benefit for bonding at all (e.g., Figure 5.3, $\bar{E}_2 h_0^{\,2} / \gamma a > 43$).

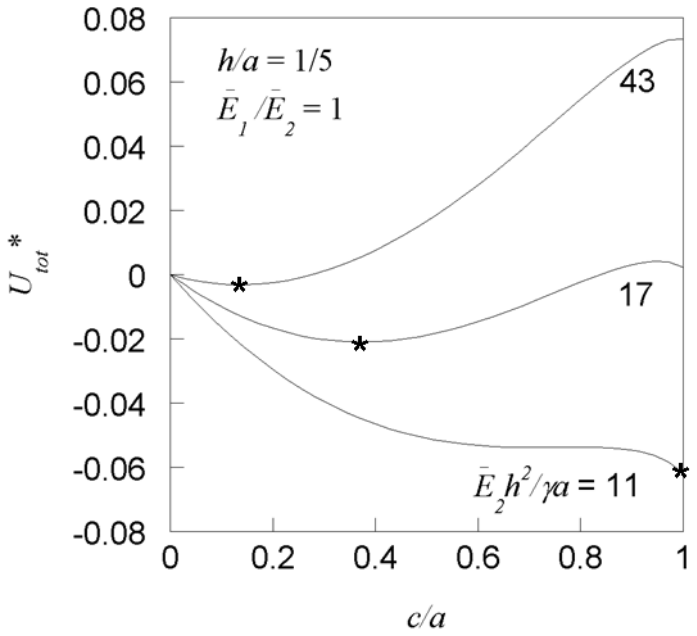

Figure 5.3 – Nondimensional energy versus extent of closure
Non-dimensional total energy versus extent of closure for unoxidized PDMS nano-channels with aspect ratio 1/5.

The extent of critical closure is marked with an asterisk on each of the U_{tot}* curves in Figure 5.3. These points from the individual curves can be translated to a plot of the critical closure distance versus the non-dimensional length scale, which is

presented in Figure 5.4. This plot provides a quick reference guide for the relative stability of a nano-channel against unwanted bonding with respect to the modulus and the surface energy of the material from which it is fabricated. The general trend outlined above for the three curves of Figure 5.3 is completely illustrated by plotting the data in this manner. The general shape of the c_c/a versus $\bar{E}_2 h_0^{\,2}/\gamma a$ curve remains the same upon varying the modulus mismatch ratio, aspect ratio of the nanochannels, and compressive stress although the details do vary.

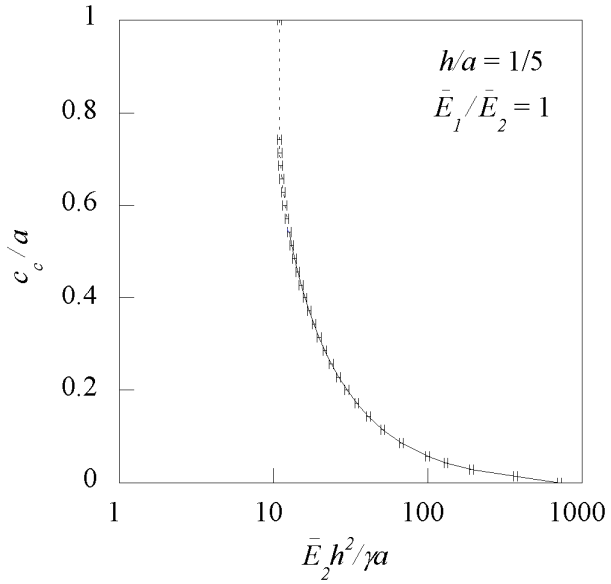

Figure 5.4 – Critical closure distance versus $\bar{E}_2 h_0^{\,2}/\gamma a$

The critical closure distance is plotted against the non-dimensional length scale $\bar{E}_2 h_0^{\,2}/\gamma a$ for unmodified PDMS nanochannels ($\bar{E}_1$ = $\bar{E}_2$) with an aspect ratio of 1:5.

5.2.2.2 Dependence on modulus-mismatch ratio

The modulus of the film that lines the nanochannels (Figure 5.1) was then varied over the range of $\bar{E}_1/\bar{E}_2$ = 1 – 190. The thickness of the film was set to h_f/h_0 = 1.7, a value which was consistent with experimental results (*62*), and the dependence on the film thickness was not further explored. Following the same method as in the previous

sub-Section, the critical closure distance was determined with respect to the non-dimensional length scale and these curves are compared against one another in Figure 5.5. Predictably, as the modulus at the surface is increased it becomes harder for the nanochannels to bond. Finally, when $\bar{E}_1/\bar{E}_2 = 190$, the non-dimensional length scale for which bonding is possible has become very small.

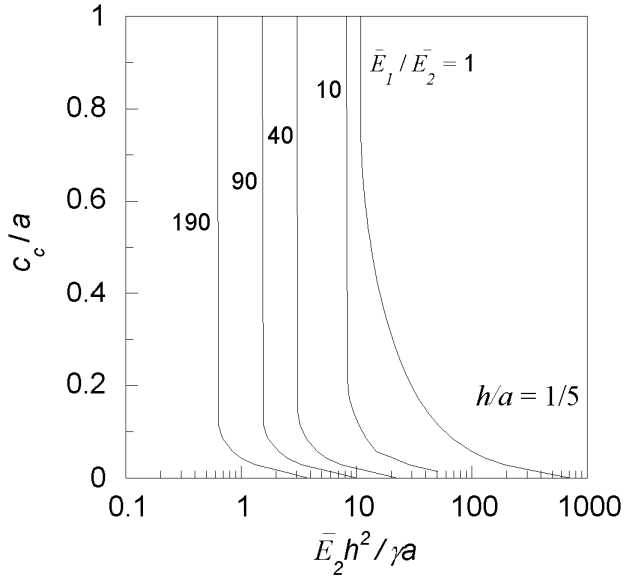

Figure 5.5 – Critical closure distance versus $\bar{E}_2 h_0^{\,2}/\gamma a$ with modulus mismatch
The critical closure distance is plotted against the non-dimensional length scale $\bar{E}_2 h_0^{\,2}/\gamma a$ again for the unmodified PDMS nanochannels ($\bar{E}_1 = \bar{E}_2$) with an aspect ratio of 1:5 as in Figure 5.4 but with the addition of the curves for a modulus mismatch ($\bar{E}_1/\bar{E}_2$) of 10, 40, 90, and 190.

Although the general behavior of the system with and without a modulus-mismatch ratio is the same, there is a detail of the U_{tot}* curves that is much more pronounced when the modulus mismatch is considered. A series of U_{tot}* versus $\bar{E}_2 h_0^{\,2}/\gamma a$ curves are presented in Figure 5.6a. For intermediate values of the non-dimensional length scale, there are two minima in each curve. Small values of non-dimensional length scale ($\bar{E}_2 h_0^{\,2}/\gamma a < \sim 9$ in Figure 5.6a) will yield only one minimum

in the curve located at *c/a* = 1. This corresponds to a nano-channel system that, without being given any perturbation, will completely collapse due to surface forces alone. Large values of non-dimensional length scale ($\overline{E}_2 h_0^{\,2}/\gamma a$ > ~13 in Figure 5.6a) will also yield only one minimum that is located close to c/a = 0. In the intermediate range of $\overline{E}_2 h_0^{\,2}/\gamma a$ there are two minima in each curve and two possible configurations of those minima: one in which the first minimum is the overall minimum and one in which the second minimum is the overall minimum. In the first case, if energy is put into the system to completely close the nano-channel it will have to be sustained to keep it closed because upon removal, the nano-channel will re-open to the value of *c/a* dictated by the first minimum. In the second case, it is predicted that the nano-channel will collapse on its own to the extent of critical closure indicated by the first minimum. However, if the necessary amount of energy is put into the system (for example, by compressing the substrate) to completely collapse the nano-channel, it will remain in the collapsed position dictated by the second minimum if the load is then removed.

The relative amounts of energy input necessary to move between the first minimum and second minimum/fully-bonded state for the full range of $\overline{E}_2 h_0^{\,2}/\gamma a$ are plotted in Figure 5.6b. The energy barrier for bonding (measured from the first minimum to the maximum of the U_{tot}* curve between the minima) starts out very small at intermediate values of $\overline{E}_2 h_0^{\,2}/\gamma a$ but increases quickly with increasing $\overline{E}_2 h_0^{\,2}/\gamma a$. Once in the fully bonded state, the energy barrier for unbonding is very large for small values of $\overline{E}_2 h_0^{\,2}/\gamma a$. However, at intermediate values of $\overline{E}_2 h_0^{\,2}/\gamma a$ there becomes relatively little resistance to unbonding.

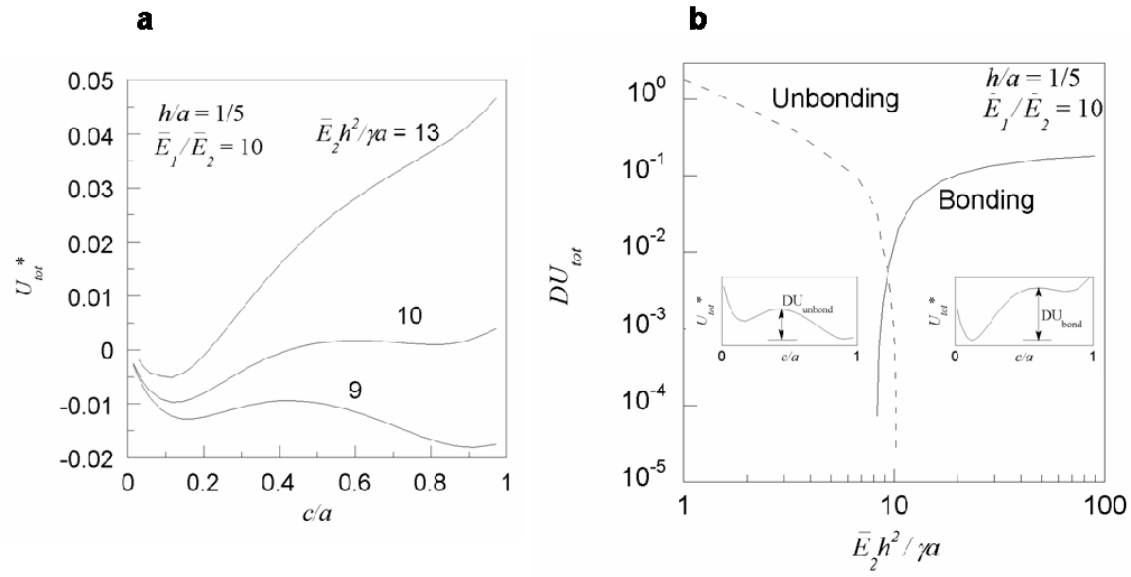

Figure 5.6 – Nondimensional energy versus extent of closure with modulus mismatch (a) The non-dimensional total energy versus extent of closure for oxidized PDMS nano-channels ($\bar{E}_1/\bar{E}_2$ = 10) with aspect ratio 1/5. (b) The relative amounts of energy necessary to move between the two minima of the total energy curves in (a).

5.2.2.3 Dependence on nano-channel aspect ratio

So far, the aspect ratio of the nano-channels has been fixed at h_0/a = 1/5, which is a relatively short triangle as compared to its base length. In Figure 5.7a, the critical closure distance is plotted against $\bar{E}_2h_0^2/\gamma a$ for different aspect ratios of unmodified nano-channels ($\bar{E}_1/\bar{E}_2$ = 1). For a given value of non-dimensional length scale, increasing the aspect ratio (increasing the height of the triangle) decreases the extent of critical closure. Therefore, as the triangular nano-channels approach an equilateral shape, a lower value of non-dimensional length scale would be required for the nano-channels to collapse. The DU_{tot}* curves for the different aspect ratios are compared in Figure 5.7b. Here it is confirmed that increasing the aspect ratio, in effect, makes it more difficult to bond the channel at equal values of $\bar{E}_2h_0^2/\gamma a$.

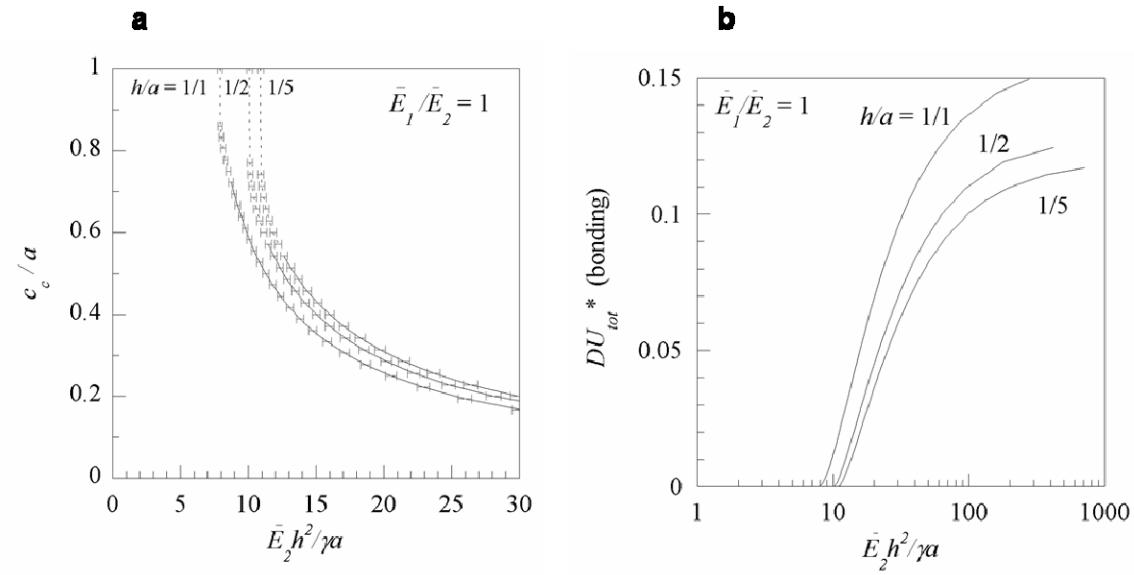

Figure 5.7 – Critical closure distance versus $\overline{E}_2 h_0^{\,2}/\gamma a$ with nanochannel aspect ratio
Critical closure distance versus nondimensional length scale, comparison of different aspect ratios of unoxidized PDMS nano-channels.

5.2.2.4 Dependence on compressive stress

In terms of controlled bonding or collapse of the nano-channel the impact of applying a compressive load is of practical importance. As expected, the effect of applying a compressive load is to increase the extent of bonding at all values of $\overline{E}_2 h_0^{\,2}/\gamma a$, shifting the entire c_c/a curve upward vertically as in Figure 5.8.

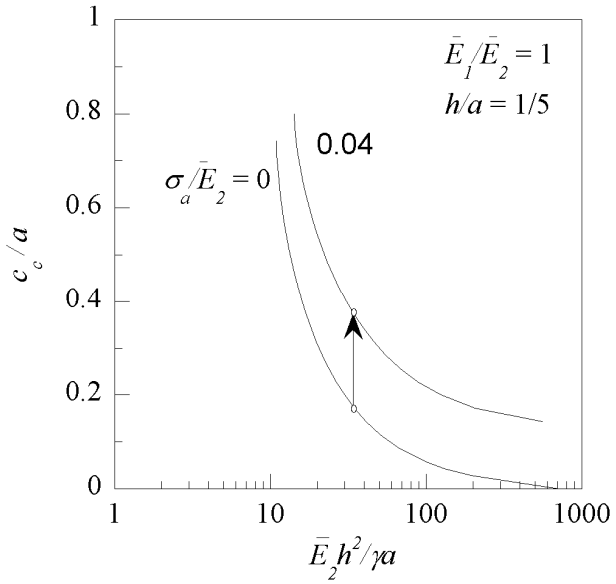

Figure 5.8 – Critical closure distance versus $\bar{E}_2 h_0^{\,2}/\gamma a$ with applied load
Critical closure distance versus non-dimensional length scale showing jump in closure when a compressive load is applied to the substrate.

5.2.2.5 Experimental observations

The closure distance curves of Figure 5.4 and 5.5 provide a critical value, for a given geometry, of $\bar{E}_2 h_0^{\,2}/\gamma a$ above which nanochannels can be supported without spontaneous collapse. For the case where the film and the substrate have the same modulus (Figure 5.4) this critical value is ~10. However, for the experimental triangular nanochannels system referenced at the beginning of this Section, $\bar{E}_2 h_0^{\,2}/\gamma a$ is approximately 1.5. It was confirmed for this system that the unmodified PDMS was unable to support open nanochannels (*7*). Furthermore, it was determined that both the compliance of the elastomer – varied by changing the ratio of polymer to curing agent – and the presence of the stiff oxidized layer were instrumental in determining if the nanochannels could be supported without spontaneous collapse. Oxidizing the most compliant PDMS (10:1) prevented some of the nanochannels from collapsing.

Ultimately, prevention of spontaneous collapse in any of the nanochannels required a mixing ratio of 3:1 with the addition of an oxidized layer. Oxidizing the PDMS to create the stiff surface-modified layer effectively decreases the critical vale of $\overline{E}_2 h_0^{\,2}/\gamma a$ as shown in Figure 5.5.

5.3 Determination and application of non-uniform surface tractions

5.3.1 Background

For the analysis of adhesion, a general issue is that one does not know *a priori* where a point from one of the surfaces will contact the other (except, for example, a pure mode I geometry), a problem that does not exist in fracture analysis where the two points are originally bonded. For this reason, the analysis presented in the previous Section is approximate for the adhesion of the ceiling of the triangular nano-channel to its base due to surface forces. Taking a closer look at the origin of the adhesion forces, it is recognized that the points of the triangular ceiling would not travel vertically downward nor would the triangular base remain stationary. The adhesion force arises as the result of molecular interactions between the sides of the triangle or, in general, two "bodies". Naturally, adhesion forces manifest themselves as body forces because they are the sum of the interactions between molecules in one body with every molecule in the second body. If the pair potential describing the energy between molecules is denoted as $w(h)$, h being the separation distance of the molecules, and the number densities of molecules on either side of the adhesion interface are ρ_1 and ρ_2, then the total interaction energy between the bodies is

$$W(h) = \int_{V_2}\int_{V_1} \rho_1 \rho_2 w(h)\, dV_1 dV_2 \,. \tag{3}$$

Since the force associated with the intermolecular pair potential is $\boldsymbol{f} = -\nabla w(h)$, the total force between the bodies becomes

$$\boldsymbol{F}(h) = \int_{V_2}\int_{V_1} \rho_1 \rho_2 \boldsymbol{f}(h)\, dV_1 dV_2 . \tag{4}$$

The interaction pair potential between molecules generally takes the form $w(h) = -C/h^n$; for example, the van der Waals interaction is described by n = 6. Due to this strong inverse dependence on separation distance, interaction forces are concentrated at the surfaces. Therefore, a significant amount of work has been dedicated to developing approximations that replace the double volume integral described above with surface integrals, which are easier to execute for either analytical or numerical solutions. Perhaps the most widely known is the Derjaguin (*81, 82*) approximation where, in its original form, the total interaction force between two bodies is computed by multiplying the interaction energy between two half-spaces, located the same distance apart as the bodies, by a geometric constant which is dependent on the radii of curvature. The Derjaguin approximation for the force between two spheres of radii R_1 and R_2 is

$$F(h)^{spheres} = 2\pi\left(\frac{R_1 R_2}{R_1 + R_2}\right) W(h)^{planes}, \tag{5}$$

where $W(h)$ is the energy per unit area of two flat surfaces at the same separation h. This approximation has also been tailored to impose surface tractions on the respective bodies, but with the geometrical limitation of needing to choose a common, or average, interaction direction as was done for the triangular nano-channels above. Argento, et al. (*83*) presented a formulation based on their development of an inter-surface stress tensor which depends on the shape of the body and the intermolecular potential. The

resulting surface tractions, at each material point are computed with respect to the surface normal of another body meaning that the direction of the surface tractions is dependent on the local curvature of the bodies.

In this Section, the development of a model for applying non-uniform surface tractions due to interaction with another body is presented. The validity of choosing such a formulation has been shown in the work of Argento, et al. (*83*). The generalized form of the model is independent of the geometry of the bodies and is based on a cohesive zone formulation. Following the discussion of the model formulation an example of its implementation is demonstrated.

5.3.2 Model development

The basis of the model is a routine for determining and assigning a non-uniform traction load to be applied to a designated surface in response to the adhesive attraction felt by the presence of a neighboring surface. Only convex or initially flat surfaces (that can be broken up to represent the boundaries of bodies for nanochannel analyses) will be considered here in order to reasonably neglect self-interactions. As surfaces with arbitrary geometries approach one another, there is a range of separation distances over which, by the action of surface forces, they are attracted to one another (Figure 5.9).

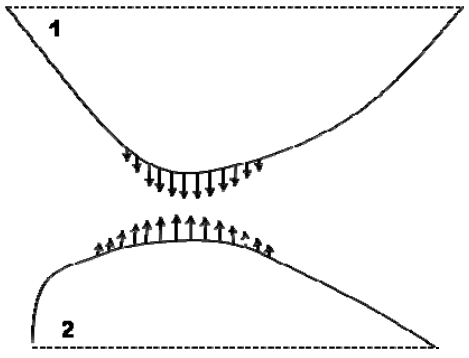

Figure 5.9 – Schematic of attractive forces between surfaces
Schematic drawing of the attraction between surfaces due to surface forces.

In the routine, the surfaces with the possibility of interacting are defined by their position. With an arbitrary geometry it is not necessarily known where the surfaces will meet. However, based on the fact that interaction forces are generally strongly inversely dependent on the separation distance, a point on one surface (the first surface) will likely move towards the other surface in the direction associated with the minimum separation distance from that point. To determine this minimum separation distance, the distances between a point on the first surface and all of the points on the second surface that can be "seen" by this point are first determined and then the minimum separation distance between the bodies from the point on the first surface is determined, h_{min}. This is repeated for many points on the first surface.

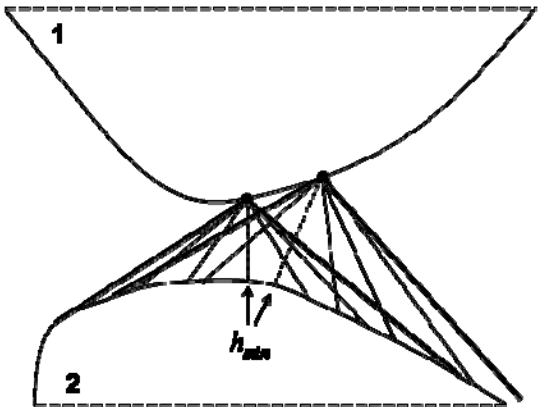

Figure 5.10 – Schematic illustration of h_{min} determination
Schematic drawing illustrating the method used for determining the minimum separation distance between several points on one body to a second body.

For every point on the first surface, a traction vector is assigned based on the minimum separation distance, $\boldsymbol{T}(h_{min})$, according to a traction-separation law. Although the method used here to compute the surface tractions is independent of the actual form of the traction-separation law, the area under the curve is equal to the surface energy. The traction assigned to each point on the first surface represents the average value of

the traction for the surface area represented by that point. To determine the traction magnitude and direction that should then be applied to the surface between points, the contributions from two neighboring points are averaged and the resulting traction is applied to the surface resulting in a distribution similar to that of Figure 5.9.

5.3.3 Implementation of the model

The adhesion model described above was implemented for the case of the adhesion of two spheres of equal radius, R. The solution to the problem of the increase in the contact area of spheres due to surface energy was established by Johnson, Kendall, and Roberts in 1971 (*84*). They based their analysis on the minimization of the total energy in the system with respect to the contact radius, a, so that the elastic energy of the deformation in and around the region of contact balances the effect of the surface energy (for zero applied load). It was determined that the resulting contact radius is dependent on the radii, the surface energy (γ), and the elastic constants of the sphere:

$$\frac{a}{R} = \left[\frac{9\pi\gamma\left(1-\nu^2\right)}{4ER} \right]^{1/3} \tag{6}$$

for the case of identical oblispheres ($R = R_1 = R_2$, $E = E_1 = E_2$, $\gamma = \gamma_1 = \gamma_2$, $\nu = \nu_1 = \nu_2$).

The traction-separation law that was chosen for this implementation is a triangular law sketched in (Figure 5.11).

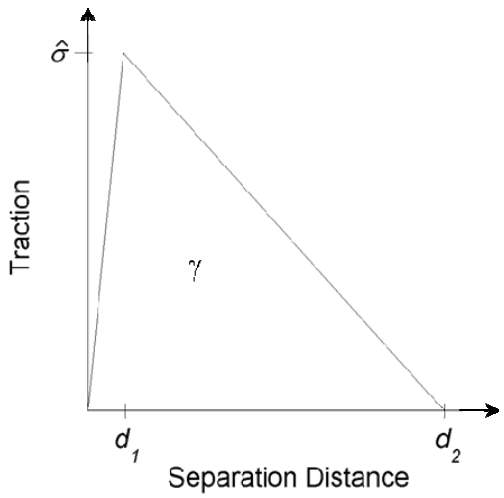

Figure 5.11 – Traction-separation law

The area under the curve, equal to the surface energy, is define by the peak stress supported between the surfaces, $\hat{\sigma}$, and the maximum separation distance for which there is an adhesive attraction between the spheres, d_2. An additional parameter in the law is the separation distance at which the peak stress occurs, d_1, which has little effect on the solution as long as it is much smaller than d_2. The use of other more strongly decaying laws (e.g., $\sigma \propto C/h^4$) was explored; however, no benefit to the solution was realized with the added complexity of the law. The solution to this problem can now be shown to be dependent on the following set of parameters:

$$a = f(\nu, E, R, d_2, \hat{\sigma}, \gamma) \tag{7}$$

However, $\gamma = f(\hat{\sigma}, d_2)$ so that the appropriate non-dimensional groups to describe this problem are

$$\frac{a}{R} = f\left(\frac{E\gamma}{\hat{\sigma}^2 R}, \nu, \frac{\gamma}{ER}\right). \tag{8}$$

The group γ/ER can be seen from Equation (6) to be the inherent parameter upon which the JKR solution depends. The other group, $E\gamma/\hat{\sigma}^2 R$, is the familiar fracture-length scale parameter for fracture analyses. For a reasonable solution, the value of this

latter group should be on the same order as the characteristic length scale of the problem.

Implementation of this method was carried out using the commercial finite-element code ABAQUS. A user subroutine was written in FORTRAN to process all of the calculations described in the previous sub-Section based on the nodal positions of the interacting surfaces (for more details on the user subroutines, please see the Appendix to this Chapter). In creating the mesh, linear axisymmetric elements were used to model a sphere (Figure 5.12a). Symmetry conditions allow for the second interacting surface to be inferred from the first. Interpenetration of the spheres was prevented with the use of rigid contact elements at the line of symmetry.

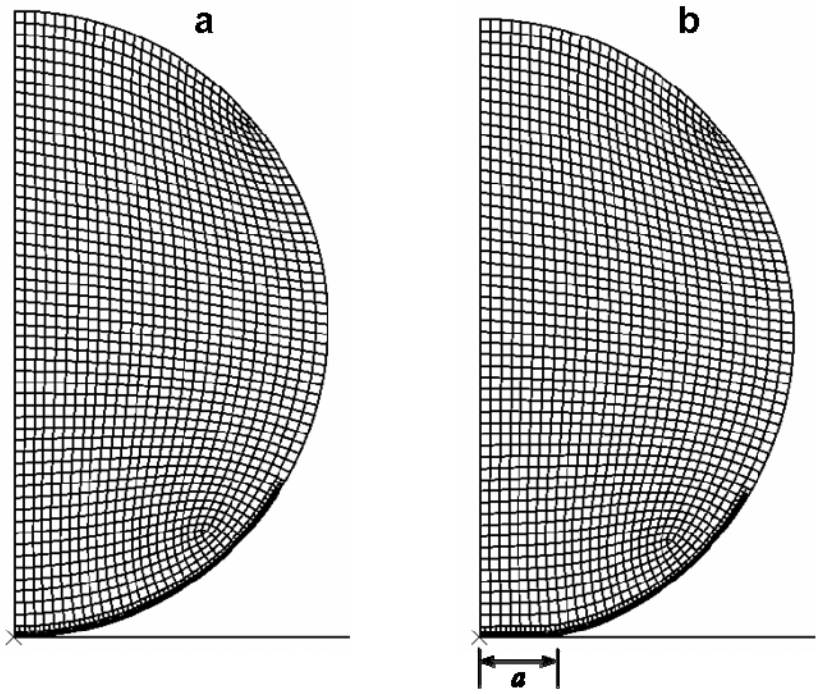

Figure 5.12 – Finite-element mesh for the contact of two spheres
Finite-element mesh a. before and b. after a non-uniform surface traction had been applied to bond the spheres due to surface energy.

The effects of the fracture-length scale on the resulting contact radius were studied and the results were compared to the contact radius predicted by the JKR theory. The model is in reasonable agreement with the JKR theory when the normalized contact radius greater than ~10^{-2} for a fracture length scale of $E\gamma/\hat{\sigma}^2 R$ = 0.15 (Figure 5.13). This corresponds to a contact radius on the same order as the fracture length scale. Increasing the fracture length scale does not provide a better fit to the JKR theory over this range, indicating that the appropriate length scale may be the contact radius and providing a possible explanation for the deviation from the JKR theory below $a/R = 10^{-2}$.

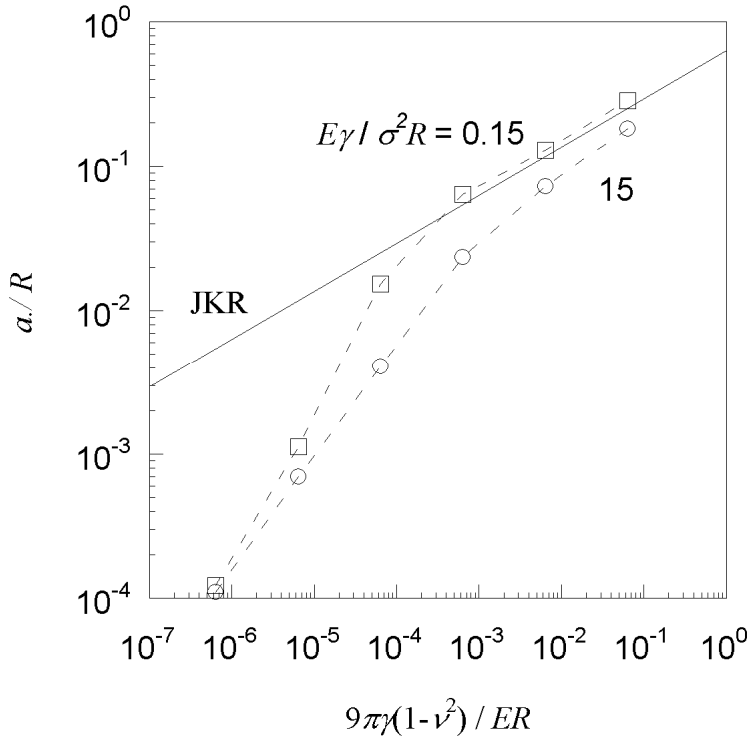

Figure 5.13 – Plot of contact radius between two spheres due to surface energy

5.4 Concluding remarks

The adhesion of nanoscale features due to the effects of surface forces has been studied in this Chapter. First, the collapse of a triangular nano-channel cross-section was investigated by computing the total energy of the system as bonding proceeded. The critical collapse distance was found to be strongly dependent on the non-dimensional length scale, $\overline{E}_2 h_0^{\,2} / \gamma a$. For a given set of material properties and nano-channel cross-sectional area, there is a critical value of $\overline{E}_2 h_0^{\,2} / \gamma a$ below which nano-channels cannot be supported. The effects of adding a stiff, surface-modified layer were studied and found to significantly decrease the critical value of $\overline{E}_2 h_0^{\,2} / \gamma a$. The effects of channel aspect ratio and applied loading were also investigated. Finally, to generalize the analysis of Section 5.2, a method was presented for determining and applying a non-uniform traction on the surface of interacting bodies. The method was demonstrated for the case of adhesive contact between spheres.

Appendix to Chapter 5

Description of ABAQUS User Subroutines

The model is constructed such that nodal input can take the form of symmetry across one plane or two planes. For example, if the adhesion of two spheres is studied, then only one symmetry plane is required. But, for the case of a void within a body, symmetry across two planes is required. The numbers of all of the nodes on the surface of the body that could possibly interact with another body are saved to an ordered node set. After an initial static stress analysis step for recording the original state of the surface nodes, a second step utilizes a call to the user subroutine UTRACLOAD. This subroutine requires information from two other user subroutines, UEXTERNALDB and URDFIL, which are called at the start of the analysis and at the end of each step for which new information has been written to the results file, respectively.

The output of the user subroutine UTRACLOAD specifies a non-uniform traction load, in the form of a magnitude and a direction, to be applied to the designated face of the element for which it is being called. In order to compute the components of the traction load for every element on the surface of the body, the current position of the surface nodes is required. The necessary nodal information is written to the results file once per increment. The subroutine URDFIL is set up to read this information and subsequently perform the necessary calculations to determine the magnitudes and directions of the traction load. Finally, that information is passed to UTRACLOAD through common block variables. UEXTERNALDB is a subroutine used to manipulate user external files and is utilized here to open a file to write pertinent information and results from the calculations taking place in URDFIL for troubleshooting purposes.

Once the node numbers, coordinates (and displacements), and connectivity data are read from the results file (the original nodes), the calculations begin with computing the appropriate set(s) of symmetric nodal coordinates. The distance between each original node and all of the symmetric nodes that the original node has the possibility of interacting with is then computed. To determine whether a particular original node and symmetric node have the possibility of interacting, the tangents to either surface, at those respective points, are computed and nodes are excluded based on which side of the intersection of the tangent with the opposite surface they lie on. The smallest distance between surfaces is then determined for each of the original nodes. A traction is assigned to this pair based on the interaction distance. The traction associated with each pair of original and symmetric nodes is broken up into global direction components. Once the traction is assigned to each original node, the contributions from both of the nodes connected to a corresponding element are averaged and the magnitude and direction components are determined and passed to the UTRACLOAD subroutine for application to that element.

Chapter 6

Conclusion

In this dissertation, some of the aspects of channel and tunnel cracking of the surface-modified layer, produced by plasma oxidation, on PDMS have been studied. Since the nanocracks, introduced by the application of a tensile strain, were shown to provide a convenient tool to produce functional patterns for investigations of behaviors such as cellular adhesion, self assembly, and nano-fluidics, it was desired to predict, or even design, crack patterns. To do this, the properties of both the PDMS substrate and the surface-modified layer as well as the thickness of the surface-modified layer needed to be determined. The first half of Chapter 2 addressed the challenges associated with measuring the properties and thickness of the surface modified layer owing to its very small size. Using the AFM, the thickness of the surface-modified layer was estimated by imaging the cross-section of surface-modified PDMS and monitoring the phase shift of the tapping-mode cantilever as it passed over the two different regions. A compliant AFM cantilever was then used to indent the surface-modified layer resulting in a linear indentation curve from which the bending stiffness of the surface-modified layer was determined. From this information it was estimated that a surface-modified layer created by four minutes of exposure to oxygen plasma (100 W) has a modulus varying

from about 37 MPa at the surface to a bulk value of 3.5 MPa at a depth of about 200 nm below the surface.

The second half of Chapter 2 reported on the cracking behavior and provided an estimate of the toughness of the surface-modified layer. The nanocracks were determined to be between approximately 1 and 8 μm apart depending on the amount of tensile strain that was applied to the system – between 30 and 5%, respectively. For a given amount of strain, some correlation was found between the spacing of the cracks and their sizes. Namely, larger cracks were found when their nearest neighbors were farther away. While the depth of the cracks could not be determined directly, it was estimated by comparing experimental observations of the crack width, surface rise, and spacing with the results of finite-element calculations that incorporated the determined properties of the surface layer. The cracks were estimated to reach between 300 and 600 nm below the surface – a depth that is greater than the estimated thickness of the surface-modified layer. Furthermore, these calculations indicated that the surface layer was essentially perfectly brittle with a toughness of about 100–300 mJ/m^2 to the depth of the cracks, the lower bound being approximately twice the reported free surface energy of oxidized PDMS. Finally, it was noted that the majority of the cracks collapsed, or healed, upon unloading.

In Chapter 3 it was shown that the crack patterns could be created on the surface of surface-modified PDMS cubes and microspheres by compression. This easy and inexpensive fabrication technique creates ordered patterns on small objects where micro-lithography, micro contact printing, or the stretch-induced patterning of Chapter 2 would be difficult to apply. The patterns were found to arise from an induced

tensile stress in the surface-modified layer upon uniaxial compression. In right prismatic shapes, such as a cube, it was determined that this tensile stress was only created if there was a mismatch in the Poisson's ratio between the surface-modified layer and the bulk or if there was friction at the contact between the compression device and the object. In contrast, for non-prismatic shapes, such as a sphere, tensile stresses could be induced simply due to their geometry. With some research into a method for the mass production of these patterned objects, they may be particularly beneficial for applications such as self-assembly.

Chapter 4 continued to explore applications for the nanocracks with the development of a method for very quickly and easily generating hundreds of parallel, size-adjustable nanochannels. Tunnel cracks, which act as nanochannels when connecting two fluidic reservoirs, were produced in the surface-modified layer that had been constrained between two PDMS substrates with the application of a tensile strain to the system. The methods from Chapter 2 were used to characterize the double-thickness of the bonded surface-modified layers which was determined to be between 450 and 1500 nm thick. The nanochannels were determined to range between approximately 400 and 1300 nm in width depending on the amount of strain that was applied to the system and be fully reversible: completely closing when the strain was released. Electrical resistance measurements made across the nanochannels when filled with a KCl solution lead to the height of the tunnel cracks being estimated to be on the order of a half of a micron. The functionality of the nanochannels was demonstrated by monitoring and controlling the flow of electrokinetically driven fluorescein molecules and electroosmotically driven quantum dots through the nanochannels.

Finally, Chapter 5 explored the adhesion (collapse or healing) of the nanocracks and nanochannels that was noted as a characteristic behavior, respectively, in Chapters 2 and 4. Based on experimental nanochannels that had previously been developed, a triangular cross-sectional nanochannel geometry was first studied. The effects of the material properties, aspect ratio, the presence and stiffness of a surface-modified layer lining the nanochannel, and the amount of remotely applied compression on the likelihood of the channel collapse were investigated. The non-dimensional length scale, $\overline{E}_2 h_0^{\,2} / \gamma a$, was found to be an important parameter in determining the amount of critical collapse of the nanochannels. The addition of the stiff, surface-modified layer was found to significantly decrease the chances of nanochannel collapse. To generalize the specific analysis of a triangular nanochannel, a method was presented for determining and applying a non-uniform traction on the surface of bodies that are interacting due to surface forces. The implementation of this method was demonstrated for the case of adhesive contact between spheres due to surface forces.

Bibliography

1. X. Y. Zhu*, et al.*, *Nat. Mater.* **4**, 403-406 (2005).

2. H. Hillborg, U. W. Gedde, *IEEE Trns. Dielectr. Electr. Insul.* **6**, 703-717 (1999).

3. J. L. Fritz, M. J. Owen, *J. Adhes.* **54**, 33-45 (1995).

4. H. Hillborg*, et al.*, *Langmuir* **20**, 785-794 (2004).

5. H. Hillborg, U. W. Gedde, *Polymer* **39**, 1991-1998 (1998).

6. A. Tóth*, et al.*, *J. Appl. Polym. Sci.* **52**, 1293-1307 (1994).

7. D. Huh*, et al.*, *Nat. Mater.* **6**, 424-428 (2007).

8. R. Huang, J. H. Prevost, Z. Y. Huang, Z. Suo, *Eng. Fract. Mech.* **70**, 2513-2526 (2003).

9. J. W. Hutchinson, Z. Suo, *Mixed-mode cracking in layered materials*, in *Advances in applied mechanics, vol 29*. 1992. p. 63-191.

10. V. B. Shenoy, A. F. Schwartzman, L. B. Freund, *Int. J. Fract.* **103**, 1-17 (2000).

11. M. D. Thouless, *J. Am. Ceram. Soc.* **73**, 2144-2146 (1990).

12. M. D. Thouless, E. Olsson, A. Gupta, *Acta Metall. Mater.* **40**, 1287-1292 (1992).

13. S. C. Glotzer, *Science* **306**, 419-420 (2004).

14. S. C. Glotzer, M. J. Solomon, *Nat. Mater.* **6**, 557-562 (2007).

15. Z. L. Zhang, A. S. Keys, T. Chen, S. C. Glotzer, *Langmuir* **21**, 11547-11551 (2005).

16. J. T. Mannion, H. G. Craighead, *Biopolymers* **85**, 131-143 (2007).

17. J. T. Mannion, C. H. Reccius, J. D. Cross, H. G. Craighead, *Biophys. J.* **90**, 4538-4545 (2006).

18. C. H. Reccius, J. T. Mannion, J. D. Cross, H. G. Craighead, *Phys. Rev. Lett.* **95**, (2005).

19. W. Reisner*, et al.*, *Phys. Rev. Lett.* **94**, (2005).

20. R. Riehn*, et al.*, *Proc. Natl. Acad. Sci. U. S. A.* **102**, 10012-10016 (2005).

21. J. O. Tegenfeldt*, et al.*, *Proc. Natl. Acad. Sci. U. S. A.* **101**, 10979-10983 (2004).

22. C. Y. Hui, A. Jagota, Y. Y. Lin, E. J. Kramer, *Langmuir* **18**, 1394-1407 (2002).

23. H. Schmid, B. Michel, *Macromolecules* **33**, 3042-3049 (2000).

24. Y. G. Y. Huang*, et al.*, *Langmuir* **21**, 8058-8068 (2005).

25. J. C. Lotters, W. Olthuis, P. H. Veltink, P. Bergveld, *J. Micromech. Microeng.* **7**, 145-147 (1997).

26. A. Bietsch, B. Michel, *J. Appl. Phys.* **88**, 4310-4318 (2000).

27. A. Kumar, H. A. Biebuyck, G. M. Whitesides, *Langmuir* **10**, 1498-1511 (1994).

28. D. C. Duffy, J. C. McDonald, O. J. A. Schueller, G. M. Whitesides, *Anal. Chem.* **70**, 4974-4984 (1998).

29. W. Gu*, et al.*, *Proc. Natl. Acad. Sci. U. S. A.* **101**, 15861-15866 (2004).

30. M. A. Unger*, et al.*, *Science* **288**, 113-116 (2000).

31. N. Bowden, W. T. S. Huck, K. E. Paul, G. M. Whitesides, *Appl. Phys. Lett.* **75**, 2557-2559 (1999).

32. K. Efimenko*, et al.*, *Nat. Mater.* **4**, 293-297 (2005).

33. H. Hillborg*, et al.*, *Polymer* **41**, 6851-6863 (2000).

34. A. K. Bhattacharya, W. D. Nix, *Int. J. Solids Struct.* **24**, 1287-1298 (1988).

35. R. Saha, W. D. Nix, *Acta Mater.* **50**, 23-38 (2002).

36. ASTM D 624-00: Standard test method for tear strength of conventional vulcanized rubber and thermoplastic elastomers. ASTM International.

37. ASTM D 5045-99: Standard test methods for plane-strain fracture toughness and strain energy release rate of plastic materials. ASTM International.

38. G. M. Whitesides*, et al.*, *Annu. Rev. Biomed. Eng.* **3**, 335-373 (2001).

39. M. Morra*, et al.*, *J. Colloid Interface Sci.* **137**, 11-24 (1990).

40. G. Bar, L. Delineau, A. Hafele, M.-H. Whangbo, *Polymer* **42**, 3627-3632 (2001).

41. MultiMode AFM Application Notes: Phase imaging: Beyond topography. Veeco Instruments, Inc.

42. F. Clement*, et al.*, *Polymer* **42**, 6259-6270 (2001).

43. S. N. Magonov, V. Elings, M.-H. Whangbo, *Surf. Sci.* **375**, L385-L391 (1997).

44. K. L. Mills*, et al.*: Properties of the surface-modified layer of plasma-oxidized poly(dimethylsiloxane), in *Mechanics of Nanoscale Materials and Devices*, edited by A. Misra, J.P. Sullivan, H. Huang, K. Lu, and S. Asif. (Mater. Res. Soc. Symp. Proc. **924E**, San Francisco, CA, 2006).

45. W. C. Oliver, G. M. Pharr, *J. Mater. Res.* **7**, 1564-1583 (1992).

46. V. P. Olshanskii, *Pmm-J. Appl. Math. Mech.* **51**, 681-683 (1987).

47. H. G. Allen: *Analysis and Design of Structural Sandwich Panels*. 1st ed., (Pergamon Press, Oxford, 1969).

48. Z. Y. Huang, W. Hong, Z. Suo, *J. Mech. Phys. Solids* **53**, 2101-2118 (2005).

49. D. Lee, N. Triantafyllidis, J. R. Barber, M. D. Thouless: *Unpublished work*, (2007).

50. W. W. Mullins, *J. Appl. Phys.* **28**, 333-339 (1957).

51. M. D. Thouless, *Acta Metall. Mater.* **41**, 1057-1064 (1993).

52. S. Jungbauer*, et al.*, *Chemphyschem* **5**, 85-92 (2004).

53. M. K. Chaudhury, G. M. Whitesides, *Langmuir* **7**, 1013-1025 (1991).

54. D. A. Bruzewicz*, et al.*, *J. Am. Chem. Soc.* **128**, 9314-9315 (2006).

55. M. Geissler, Y. N. Xia, *Adv. Mater.* **16**, 1249-1269 (2004).

56. K. E. Paul, M. Prentiss, G. M. Whitesides, *Adv. Funct. Mater.* **13**, 259-263 (2003).

57. Y. N. Xia, J. Tien, D. Qin, G. M. Whitesides, *Langmuir* **12**, 4033-4038 (1996).

58. R. J. Jackman, J. L. Wilbur, G. M. Whitesides, *Science* **269**, 664-666 (1995).

59. O. Cayre, V. N. Paunov, O. D. Velev, *J. Mater. Chem.* **13**, 2445-2450 (2003).

60. H. Y. Chen, J. M. Rouillard, E. Gulari, J. Lahann, *P. Natl. Acad. Sci. USA* **104**, 11173-11178 (2007).

61. Z. N. Bao*, et al.*, *Chem. Mater.* **14**, 24-+ (2002).

62. K. L. Mills, X. Zhu, S. Takayama, M. D. Thouless, *J. Mater. Res.* **23**, 37-48 (2008).

63. K. B. Jirage, J. C. Hulteen, C. R. Martin, *Science* **278**, 655-658 (1997).

64. S. B. Lee*, et al.*, *Science* **296**, 2198-2200 (2002).

65. S. M. Stavis, J. B. Edel, K. T. Samiee, H. G. Craighead, *Lab Chip* **5**, 337-343 (2005).

66. J. P. Fu*, et al.*, *Nat. Nanotech.* **2**, 121-128 (2007).

67. J. Han, H. G. Craighead, *Science* **288**, 1026-1029 (2000).

68. P. Muller-Buschbaum*, et al.*, *Appl. Phys. Lett.* **88**, (2006).

69. P. Sivanesan*, et al.*, *Anal. Chem.* **77**, 2252-2258 (2005).

70. Y. N. Xia, G. M. Whitesides, *Annu. Rev. Mater. Sci.* **28**, 153-184 (1998).

71. S. Ho, Z. Suo, *J. Appl. Mech.-Trans. ASME* **60**, 890-894 (1993).

72. S. Ho, Z. Suo, *Acta Metall. Mater.* **40**, 1685-1690 (1992).

73. A. Parvizi, K. W. Garrett, J. E. Bailey, *J. Mater. Sci.* **13**, 195-201 (1978).

74. D. C. Duffy, J. C. McDonald, O. J. A. Schueller, G. M. Whitesides, *Anal. Chem.* **70**, 4974-4984 (1998).

75. F. Katzenberg, *E-Polymers*, (2005).

76. S. Bhattacharya, A. Datta, J. M. Berg, S. Gangopadhyay, *J. Microelectromech. S.* **14**, 590-597 (2005).

77. G. Drazer, J. Koplik, A. Acrivos, B. Khusid, *Phys. Rev. Lett.* **89**, (2002).

78. W. Zhou*, et al.*, *Appl. Phys. Lett.* **87**, (2005).

79. M. M. J. Decre, P. H. M. Timmermans, O. van der Sluis, R. Schroeders, *Langmuir* **21**, 7971-7978 (2005).

80. K. G. Sharp*, et al.*, *Langmuir* **20**, 6430-6438 (2004).

81. B. Derjaguin, *Kolloid-Zeitschrift* **69**, 155-164 (1934).

82. J. N. Israelachvili: *Intermolecular and Surface Forces*. 2nd ed., (Academic Press, San Diego, 1991).

83. C. Argento, A. Jagota, W. C. Carter, *J. Mech. Phys. Solids* **45**, 1161-1183 (1997).

84. K. L. Johnson, K. Kendall, A. D. Roberts, *Proc. R. Soc. London Ser. A-Math. Phys. Eng. Sci.* **324**, 301-& (1971).